

High-latitude stratospheric aerosol injection to preserve the Arctic

Lee Walker Raymond¹, MacMartin Douglas G¹, Vioni Daniele², Kravitz Ben³, Chen Yating⁴, Moore John Christopher⁴, Leguy Gunter⁵, Lawrence David M⁶, and Bailey David Anthony⁶

¹Cornell University

²Sibley School of Mechanical and Aerospace Engineering, Cornell University

³Indiana University

⁴Beijing Normal University

⁵National Center for Atmospheric Research

⁶National Center for Atmospheric Research (UCAR)

November 16, 2022

Abstract

Stratospheric aerosol injection (SAI) has been shown in climate models to reduce some impacts of global warming in the Arctic, including the loss of sea ice, permafrost thaw, and reduction of Greenland Ice Sheet (GrIS) mass; SAI at high latitudes could preferentially target these impacts. In this study, we use the Community Earth System Model to simulate two Arctic-focused SAI strategies, which inject at 60°N latitude each spring with injection rates adjusted to either maintain September Arctic sea ice at 2030 levels (“Arctic Low”) or restore it to 2010 levels (“Arctic High”). Both simulations maintain or restore September Arctic sea ice to within 10% of their respective targets, reduce permafrost thaw, and increase GrIS surface mass balance by reducing runoff. Arctic High reduces these impacts more effectively than a globally-focused SAI strategy that injects similar quantities of SO₂ at lower latitudes. However, Arctic-focused SAI is not merely a “reset button” for the Arctic climate, but brings about a novel climate state, including changes to the seasonal cycles of Northern Hemisphere temperature and sea ice and less high-latitude carbon uptake relative to SSP2-4.5. Additionally, while Arctic-focused SAI predominantly cools the Arctic, its effects are not confined to the Arctic, including detectable cooling throughout most of the northern hemisphere for both simulations, increased mid-latitude sulfur deposition, and a southward shift of the location of the Intertropical Convergence Zone (ITCZ).

High-latitude stratospheric aerosol injection to preserve the Arctic

Walker Raymond Lee¹, Douglas G. MacMartin¹, Daniele Visioni¹, Ben Kravitz^{2,3}, Yating Chen⁴, John C. Moore^{4,5,6}, Gunter Leguy⁷, David M. Lawrence⁷, David A. Bailey⁷

¹Sibley School for Mechanical and Aerospace Engineering, Cornell University, Ithaca, NY, USA

²Department of Earth and Atmospheric Science, Indiana University, Bloomington, IN, USA

³Atmospheric Sciences and Global Change Division, Pacific Northwest National Laboratory, Richland, WA, USA

⁴College of Global Change and Earth System Science, Beijing Normal University, Beijing, 100875, China

⁵CAS Center for Excellence in Tibetan Plateau Earth Sciences, Beijing, 100101, China

⁶Arctic Centre, University of Lapland, Rovaniemi, Finland

⁷Climate and Global Dynamics Laboratory, National Center for Atmospheric Research, Boulder, CO, USA

Key Points:

- Stratospheric aerosol injection at high latitudes could preferentially reduce the impacts of global warming in the Arctic
- Simulated injection of SO₂ at 60N increases sea ice and permafrost extents and preserves Greenland ice sheet mass
- High latitude injection preserves the Arctic more efficiently than tropical injection but also substantially affects tropical precipitation

Corresponding author: Walker Raymond Lee, w1644@cornell.edu

Abstract

Stratospheric aerosol injection (SAI) has been shown in climate models to reduce some impacts of global warming in the Arctic, including the loss of sea ice, permafrost thaw, and reduction of Greenland Ice Sheet (GrIS) mass; SAI at high latitudes could preferentially target these impacts. In this study, we use the Community Earth System Model to simulate two Arctic-focused SAI strategies, which inject at 60°N latitude each spring with injection rates adjusted to either maintain September Arctic sea ice at 2030 levels (“Arctic Low”) or restore it to 2010 levels (“Arctic High”). Both simulations maintain or restore September Arctic sea ice to within 10% of their respective targets, reduce permafrost thaw, and increase GrIS surface mass balance by reducing runoff. Arctic High reduces these impacts more effectively than a globally-focused SAI strategy that injects similar quantities of SO₂ at lower latitudes. However, Arctic-focused SAI is not merely a “reset button” for the Arctic climate, but brings about a novel climate state, including changes to the seasonal cycles of Northern Hemisphere temperature and sea ice and less high-latitude carbon uptake relative to SSP2-4.5. Additionally, while Arctic-focused SAI predominantly cools the Arctic, its effects are not confined to the Arctic, including detectable cooling throughout most of the northern hemisphere for both simulations, increased mid-latitude sulfur deposition, and a southward shift of the location of the Intertropical Convergence Zone (ITCZ).

Plain Language Summary

The injection of reflective particles called sulfate aerosols into the atmosphere to reflect sunlight, commonly called “stratospheric aerosol injection” (SAI) or simply “geo-engineering”, could be used alongside emission cuts and CO₂ removal to cool the planet and reduce global warming. Concentrating this particle injection at high latitudes could be used to preserve the Arctic. We simulate such “Arctic-focused” geoengineering and find that it does indeed preserve sea ice, permafrost, and the Greenland Ice Sheet. However, focusing on the Arctic also introduces complications: large quantities of carbon are stored by plants at mid-to-high latitudes, and cooling the Arctic may reduce their ability to take up carbon from the atmosphere. Additionally, cooling just the Arctic could affect the way heat is transported around the planet, changing important precipitation patterns in the tropics. Finally, most of the injected sulfur would come back down in the highly-populated middle latitudes and the relatively pristine high latitudes, likely affecting ecosystems in both regions.

1 Introduction

The Arctic is especially vulnerable to global warming; high latitudes respond more strongly to external forcing than the rest of the planet by a factor of two to four, a phenomenon referred to as Arctic amplification (Previdi et al., 2021; England et al., 2021; Pithan & Mauritsen, 2014), and this faster warming in the Arctic is predicted to have consequences for the rest of the world. The extent of sea ice, which insulates the ocean from sunlight and plays crucial dynamic and thermodynamic roles in the Arctic climate and ecosystems, has decreased in all months of the year over the 1980-2018 period (Stroeve & Notz, 2018), and there is a very high likelihood that the Arctic Ocean will become ice-free in summertime before mid-century (Notz & Stroeve, 2018). Permafrost - perennially-frozen soil at high latitudes - contains an estimated 1300 Pg (Hugelius et al., 2014) to 1600 Pg (Tarnocai et al., 2009) of carbon, with approximately 500 Pg of this reservoir contained in the topmost meter of soil (1 Pg = 1 Gt = 10¹⁵ g). Globally, permafrost temperatures have increased by an average of 0.29°C over the last two decades (Biskaborn et al., 2019), and as permafrost thaws under strong warming scenarios, an estimated 5-15% or more of the carbon contained in the permafrost zone may decompose and be released into the atmosphere as CO₂ or CH₄ (Schuur et al., 2015; Plaza et al., 2019). Lastly,

the mass balance of the Greenland Ice Sheet (GrIS) has transitioned from approximately neutral in the 1990s to increasingly negative over the past 20 years (Bamber et al., 2018). The observed annual contribution of the GrIS to global mean sea level rise has increased since the 1990s (Mouginot et al., 2019), and the IPCC's 6th Assessment Report estimates that the GrIS will likely contribute a total of 1-10 cm of sea level rise by 2100 under a low-emissions scenario and 9-18 cm under a high-emissions scenario (Fox-Kemper et al., 2021).

The artificial reflection of sunlight to cool the earth's surface, referred to henceforth as solar radiation modification (SRM) but also varyingly called solar geoengineering, climate engineering, solar radiation management, or solar climate intervention, has been proposed as a possible additional response to global warming alongside emission mitigation and carbon dioxide removal. Of the proposed methods of SRM, the best understood is stratospheric aerosol injection (SAI), which aims to mimic the global cooling that follows large volcanic eruptions. The effects of SAI on the surface climate depend on the latitude(s) of injection; therefore, the question of SAI is not just whether or not to deploy, but also how. The majority of SAI simulations thus far use low-latitude injections (e.g., 30° and 15°N and S) to cool the planet relatively evenly (Kravitz et al., 2017; Tilmes et al., 2018, 2020; MacMartin & Kravitz, 2019; MacMartin et al., 2022; Richter et al., 2022); such "globally-focused" strategies have been found to preserve sea ice, and they can even be designed with sea ice preservation as a primary goal (W. Lee et al., 2020). Low-latitude SAI could also slow the degradation of permafrost and mitigate carbon loss (Chen et al., 2020; H. Lee et al., 2019) and preserve Greenland ice sheet mass (Moore et al., 2019). However, an "Arctic-focused" strategy (for example, injecting at 60°N in the springtime), could more efficiently cool the high latitudes with less cooling at lower latitudes, thus preferentially targeting impacts in or near the Arctic (Robock et al., 2008; W. Lee et al., 2021). However, Arctic-focused SAI could also introduce complications; for example, hemispherically asymmetric cooling could push the ITCZ towards the opposite hemisphere, impacting tropical precipitation (Haywood et al., 2013; Krishnamohan & Bala, 2022), and both Robock et al. (2008) and Jackson et al. (2015) observed such a disruption in the summer monsoons for high-latitude injection. Additionally, local impacts such as sulfur deposition would impact ecosystems and the people who live in them. Timely research of the physical impacts of SAI is crucial to inform future decision-making (National Academies of Sciences, Engineering, and Medicine, 2021); however, Arctic-focused SAI has received comparatively less research attention relative to globally-focused strategies. Robock et al. (2008) compared tropical and high-latitude injections to observe the effects on surface temperature, precipitation, and sea ice, but the injection amounts were relatively small and the study only considered 10-year averages for many of its results, making the signal-to-noise ratio quite low. That study also injected year-round for both strategies, whereas spring injection has been found to be more efficient for high-latitude injection (W. Lee et al., 2021). Additionally, climate models have evolved substantially over the past 15 years; for example, Robock et al. (2008) used a bulk aerosol treatment, whereas many present-day models use more complex modal treatments. Jackson et al. (2015) found that Arctic sea ice could be recovered with springtime high-latitude injection, but the primary focus of that study was to assess the controllability of Arctic sea ice rather than to diagnose the effects of SAI; those simulations introduced additional noise to the model output, added several explosive volcanic eruptions, and made random changes to the timing of injection to challenge the control algorithms. Beyond surface temperature, precipitation, and sea ice, the other possible impacts of Arctic-focused SAI (such as permafrost and GrIS surface mass balance) remain largely unanalyzed.

While large, hemispherically-asymmetric injections may ultimately prove untenable due to the possible effects on tropical precipitation, it is plausible that an SAI strategy could include some amount of injection at 60°N, possibly alongside Antarctic or tropical southern hemisphere injection. Simulating Arctic-focused SAI is important to begin i) understanding the effects of SAI on the Arctic, and ii) quantifying possible side-

effects, such as changes to tropical precipitation. In this study, we aim to provide a comprehensive analysis of Arctic-focused SAI by simulating two high-latitude injection strategies and comparing them to three globally-focused strategies. Section 2 describes our methodology, including the climate model and experimental design process. In Section 3, we investigate how our strategies affect the climate system: we begin by diagnosing changes to shortwave (SW) and longwave (LW) energy budgets, and we then analyze the effects of our strategies on the Arctic and global surface environments, including sea ice extent, permafrost carbon flux, GrIS mass, surface temperature, and precipitation. In Section 4, we present our conclusions and discuss the implications of our research for future work. Additional results (including effects on ozone and the Atlantic Meridional Overturning Circulation) and information about statistical methods and feedback algorithm design are documented in the Supporting Information (SI).

2 Methods

2.1 Climate Model

Our simulations are conducted using version 2 of the Community Earth System Model (CESM2, described by Danabasoglu et al. (2020)) with version 6 of the Whole Atmosphere Community Climate Model (WACCM6, described by Gettelman et al. (2019)) as the atmospheric component, run using the “middle atmosphere” (MA) chemistry mechanism to improve computational efficiency by greatly reducing the tropospheric chemistry scheme. We denote this configuration as CESM2(WACCM-MA). The configuration is the same as that used by the globally-focused strategies of MacMartin et al. (2022), to which we will compare our Arctic-focused simulations. CESM2 is a state-of-the-art Earth System Model with fully-coupled atmosphere, ocean, land, sea ice, land ice, river, and wave components, and WACCM6 has a horizontal resolution of 0.95° latitude \times 1.25° longitude and 70 vertical model levels extending up to 140 km, or 4.5×10^{-6} hPa. CESM2(WACCM6) performs well in modeling sea ice behavior relative to observations; it matches observed seasonal cycles and decreasing trends of sea ice extent and volume (DuVivier et al., 2020) and matches historical sea ice extent and volume observations as well as or better than any other model in Phase 6 of the Coupled Model Intercomparison Project (Notz & SIMIP, 2020). The middle atmosphere variant of CESM2(WACCM6) used here is similar to configurations of CESM1(WACCM) (Mills et al., 2017) used in the Geoengineering Large Ensemble (GLENS) project (Kravitz et al., 2017; Tilmes et al., 2018).

WACCM6 uses version 4 of the Modal Aerosol Model (MAM4), which uses a three-bin aerosol distribution system and has been validated against in-situ observations (Liu et al., 2016; Mills et al., 2017). The oceanic component is version 2 of the Parallel Ocean Program (POP2, Smith et al. (2010); Danabasoglu et al. (2012)); the land component is version 5 of the Community Land Model (CLM5, Lawrence et al. (2019)); and the sea ice component is version 5.1.2 of the Los Alamos Sea Ice Model (CICE5, Hunke et al. (2015)). The land ice component is version 2.1 of the Community Ice Sheet Model (CISM2, Lipscomb et al. (2019)), which is run over Greenland at a 4-km resolution. Surface temperature and surface mass balance for glaciated cells are computed in CLM5, downscaled to the finer resolution through linear (vertical) and bilinear (horizontal) interpolation, and passed to CISM2 through the coupler. CISM2 is run with one-way coupling, meaning the GrIS does not evolve, and the mass changes therefore exclude ice dynamics.

2.2 Simulation Design

Our Arctic Low and Arctic High simulations each begin in the year 2035, branching from the SSP2-4.5 scenario, and end at the beginning of 2070. SSP2-4.5 has three ensemble members; Arctic Low and Arctic High both branch from the first member, but all three ensemble members are used for analysis in subsequent sections except for plots of cloud optical depth and sulfur deposition, for which only the data from the first mem-

Table 1. Simulation Parameters

Name	Inj. Latitude	Inj. Months	Target ^a	Ref. Period ^b
Arctic Low	60°N	MAM ^c	1.98 million km ²	2020-2039
Arctic High	60°N	MAM	4.45 million km ²	2000-2019
Global+1.5	30°N/15°N/15°S/30°S	All	288.5 K	2020-2039
Global+1.0	30°N/15°N/15°S/30°S	All	288.0 K	2007-2028
Global+0.5	30°N/15°N/15°S/30°S	All	287.5 K	1993-2012

^aSeptember sea ice extent (if millions km²) or global mean temperature (if K)

^bPeriod of Historical/SSP2-4.5 when the average of the target metric equals the target value

^cMarch, April, May

ber was saved. Each SSP2-4.5 ensemble member begins in 2015, branching from three respective ensemble members of a Historical simulation. The SSP2-4.5 background, simulation length, and start date are chosen to allow comparison with the globally-focused strategies of MacMartin et al. (2022), which also use CESM2(WACCM-MA) and have the same background, duration, and start date. 35 years of model output is sufficiently long to account for a transient period (15 years) at the beginning of the simulation after SAI is first introduced while still providing 20 years for analysis.

Both Arctic High and Arctic Low use SAI to regulate the extent of Northern Hemisphere September sea ice (SSI) by injecting at 60°N in springtime, approximately 5 km above the tropopause, as in W. Lee et al. (2021). W. Lee et al. (2021) found that concentrating the injection in the springtime approximately doubles the effect of SAI on SSI recovery relative to year-round injection. We implement our injection strategy by placing SO₂ into the 60.6°N, 180°E grid box bounded by the 110 and 130 hPa pressure interfaces (corresponding to an altitude of approximately 14.7-14.9 km) during March, April, and May (MAM) in each year of simulation. For Arctic Low, the target September sea ice extent is the 2020-2039 SSP2-4.5 average (first ensemble member only) in the CESM2(WACCM6-MA) configuration, equal to 1.98 million km²; this “reference period” is the same as those of MacMartin et al. (2022). For Arctic High, we choose a higher target, which is the 2000-2019 Historical and SSP2-4.5 average (4.45 million km², also using only the first ensemble member). Simulation details are summarized in Table 1.

The quantity of SO₂ injected each year is chosen by a control algorithm (MacMartin et al., 2014; Kravitz et al., 2017); each year of simulation, the algorithm calculates the amount of SO₂ needed in order to restore sea ice to the target extent. The algorithm consists of a feedforward and a feedback component: the feedforward component prescribes a linearly increasing injection rate chosen based on the best guess of the injection required to maintain the target sea ice extent, and the feedback component corrects for uncertainty by adjusting the injection rate each year based on the performance of the controller. The feedforward and feedback gains are derived from the changes in sea ice extent in the MAM-60 simulation of W. Lee et al. (2021) relative to the background simulation (RCP8.5); while those simulations use an earlier version of the climate model as well as a different forcing scenario, the feedback term in our algorithm corrects for any uncertainty, and our results demonstrate that this is sufficient to control for sea ice despite the difference in model versions. The feedforward gains used for our simulations are 0.272 Tg/yr for Arctic Low and 6.109 Tg + 0.272 Tg/yr for Arctic High (with the offset in the Arctic High case to account for the sea ice difference between the reference time period of 2000-2020 and the first year of the simulation); the feedback gain used for both simulations is 0.491 Tg per year per million km² (i.e., the injection quantity each year is adjusted up or down by 0.491 Tg for each million km² of the total time-integrated difference be-

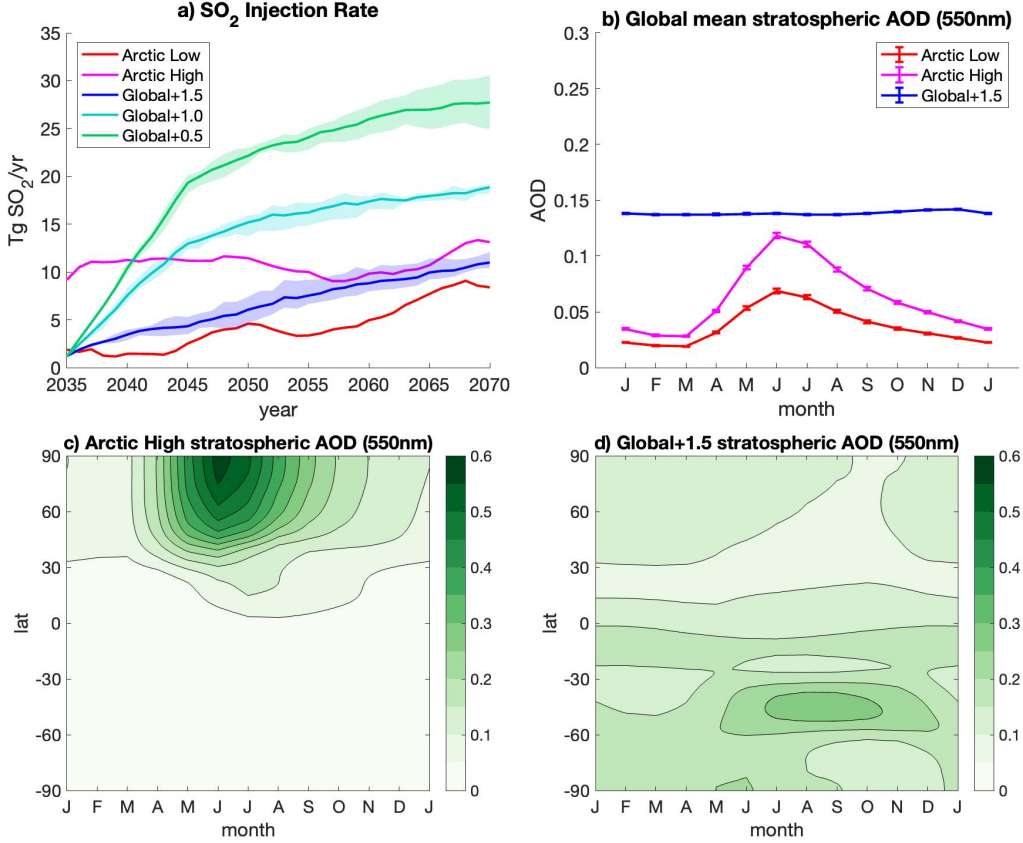


Figure 1. SO₂ injection rates and stratospheric aerosol optical depth (AOD) at the 550nm wavelength for the Arctic Low and Arctic High simulations, with comparison to global strategies described in MacMartin et al. (2022). Panel (a) plots injection rate as a function of time; shading denotes ensemble spread. Panel (b) plots seasonal cycles of global mean 550nm stratospheric AOD, averaged over the 2050-2069 period; error bars denote standard error as described in Text S2. Panels (c) and (d) plot seasonal cycles of zonal mean 550nm stratospheric AOD for Arctic High and Global+1.5, respectively, averaged over the 2050-2069 period.

tween model output and the target). The algorithm design process is described in more detail in Text S1.

In Figure 1, we present SO₂ injection rate and stratospheric aerosol optical depth (AOD) data for our simulations of Arctic-focused SAI, alongside globally-focused simulations from MacMartin et al (2022). Shading and error bars in Fig. 1 and subsequent figures denote standard error as defined in Text S2 of the Supporting Information. The globally-focused simulations considered here all inject year-round at 30°N, 15°N, 15°N, and 30°S to control global mean temperature (T0), the interhemispheric temperature gradient (T1), and the equator-to-pole temperature gradient (T2). The three simulations have global mean temperature targets of 1.5°C, 1.0°C, and 0.5°C above preindustrial conditions, respectively; we refer to them here as “Global+1.5,” “Global+1.0,” and “Global+0.5,” respectively. Each has three ensemble members. Averaged over the last 20 years of simulation (2050-2069), Arctic Low injects 5.57 ± 0.09 Tg/yr, Arctic High injects 10.66 ± 0.10 Tg/yr, and Global+1.5 injects 8.58 ± 0.04 Tg/yr (\pm denotes standard error as in Text S2 of the Supporting Information). Compared to the Global+1.5 ensemble aver-

age, Arctic High and Arctic Low produce less than half and less than a quarter, respectively, of the area-weighted, globally-averaged, annual mean AOD (0.06 and 0.03 compared to 0.14). However, for latitudes above 60°N , Arctic High and Arctic Low AODs are twice as large as Global+1.5 and comparable to Global+1.5, respectively (0.24 and 0.14 compared to 0.12). Averaged only over June, July, and August, the high-latitude AOD for Arctic High and Arctic Low approximately doubles relative to year-round, whereas Global+1.5 is unchanged (0.44 and 0.25 compared to 0.12).

3 Results

3.1 Changes to Radiative Fluxes

A starting point for understanding how the increased AOD in Fig. 1c affects the climate system is to evaluate the net changes in shortwave (SW) radiative fluxes. These are determined not only by the addition of the aerosols, but also by resulting changes in surface albedo (primarily increases in snow and ice extent at high latitudes) that amplify the initial forcing, and changes in cloud cover that both reduce the net forcing and change the spatial distribution. In Figure 2, we present changes to shortwave (SW) radiative fluxes for Arctic High relative to SSP2-4.5, averaged over the 2050-2069 period; the figure also plots changes to atmospheric sulfur burden, surface albedo, and cloud optical depth, which affect SW forcing. The peak sulfur concentration is found closest to the pole (Fig. 2i); this correlates to the AOD distribution in Figure 1c, as well as to changes in clearsky (i.e., in the absence of clouds) downwelling surface SW flux, which is highest at high latitudes (2g) (this is also affected by changes in atmospheric water vapor and ozone). The net change in top-of-model (TOM) SW fluxes is strongly affected by surface albedo changes that also peak at high latitudes (2k); considering clearsky fluxes only, the net TOM SW change at high latitudes is roughly double the change in downwelling surface SW forcing (compare 2c and 2g). However, the pole has very little surface area; both the zonally-integrated sulfur content (2j) and the total change in top-of-model clearsky SW energy per degree of latitude (2d) are largest south of the injection location rather than over the Arctic.

These changes are then further modified by changes in cloud cover. Changes to full-sky top-of-model forcing (2a, 2b) are either identical to or smaller than changes to clearsky top-of-model forcing (2c, 2d) in magnitude everywhere in the northern hemisphere, showing that as a whole, changes in cloud cover dampen changes to forcing. Full-sky SW changes in the tropics form a “zig-zag” that is absent in clearsky SW changes; these changes are predominantly due to changes in cloud cover associated with a southward shift in the ITCZ (discussed in Section 3.3; see Fig. 9). Lastly, at high latitudes, after accounting for cloud changes, downwelling SW at the surface (2e, 2f) actually increases at high latitudes despite the increased sulfur burden and AOD; this change is absent in the clearsky flux (2g, 2h), indicating that reduced clouds under SAI (2l) allow more SW to reach the surface. The largest reduction in surface downward SW is therefore in the mid-latitudes. This is consistent the results of Robock et al. (2008), which also reported the largest reduction in net surface SW south of the injection site for Arctic injection at 68°N .

Changing the energy coming into the climate system will also affect the energy going out; surface temperature affects the LW energy emitted at the surface, and changes to clouds and humidity affect how that energy is transmitted through the atmosphere. In Fig. 3, we plot changes to surface and top-of-model LW fluxes; also shown are changes to near-surface temperature and humidity. Surface temperature changes (3c) are largest at high latitudes, corresponding to reduced LW emitted at the surface (3a); however, as with SW fluxes, zonally-integrated changes to emitted LW peak in the mid-latitudes (3b). Increases in sea ice extent under SAI (see Fig. 4 and accompanying discussion) play a role in this process, as warmer water now covered by colder sea ice decreases upwelling LW at the surface. Arctic High also reduces near-surface humidity in the northern hemi-

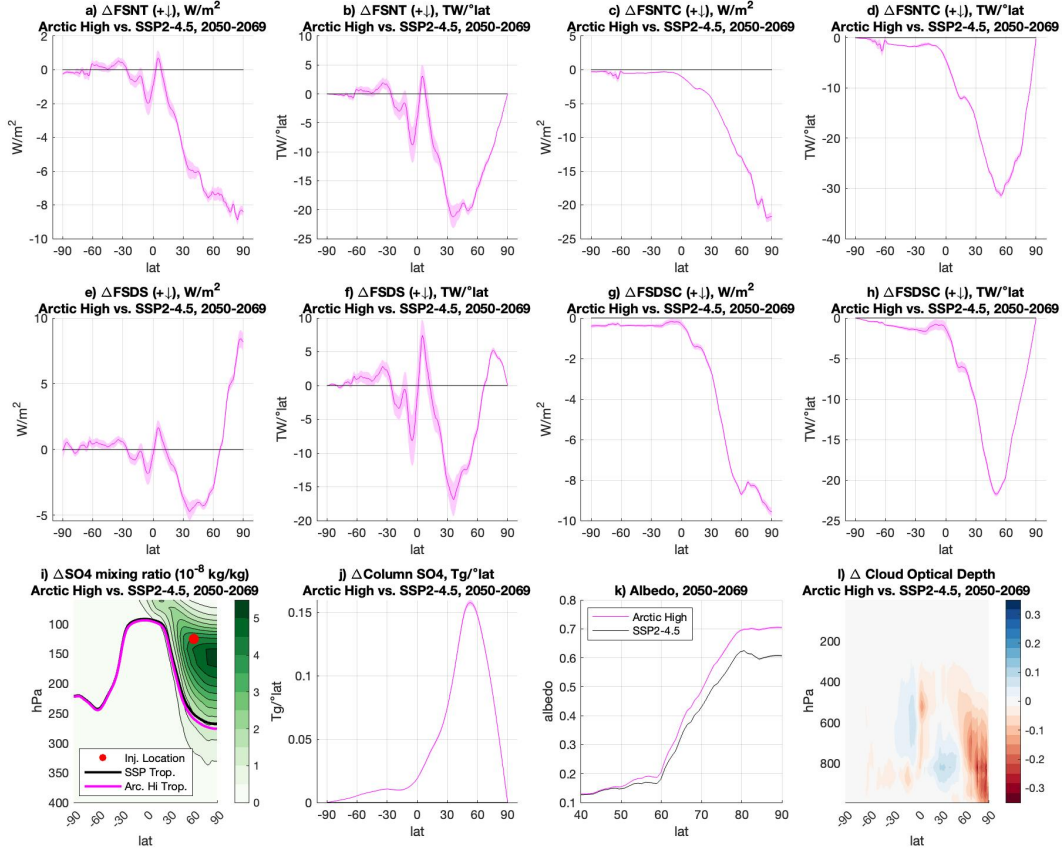


Figure 2. Changes to shortwave (SW) fluxes, SO_4 burden, surface albedo, and cloud optical depth for Arctic High relative to SSP-2.45, averaged over 2050-2069. The top row shows changes to top-of-model downwelling SW fluxes, and the middle row shows changes to surface downwelling SW fluxes (positive downward for all); the left two columns show "full-sky" fluxes (considering clouds), and the right two columns show "clearsky" fluxes (without clouds). Changes to each of these fluxes are shown both as a zonal mean in W/m^2 (columns 1 and 3) and as a zonal integral in TW per degree latitude (columns 2 and 4). The bottom left panels show the distribution of changes to atmospheric SO_4 burden; panel (i) shows zonal mean changes to mixing ratio across latitude and altitude (injection location and tropopause locations for Arctic High and SSP2-4.5 are included for reference), and panel (j) shows changes to altitude-integrated, zonally integrated column SO_4 . Panel (k) shows changes to zonal mean surface albedo across 40°N - 90°N . Panel (l) shows changes to gridbox cloud SW optical depth (only one ensemble member for SSP2-4.5). All shading for 20-year averages denotes standard error as described in Text S2.

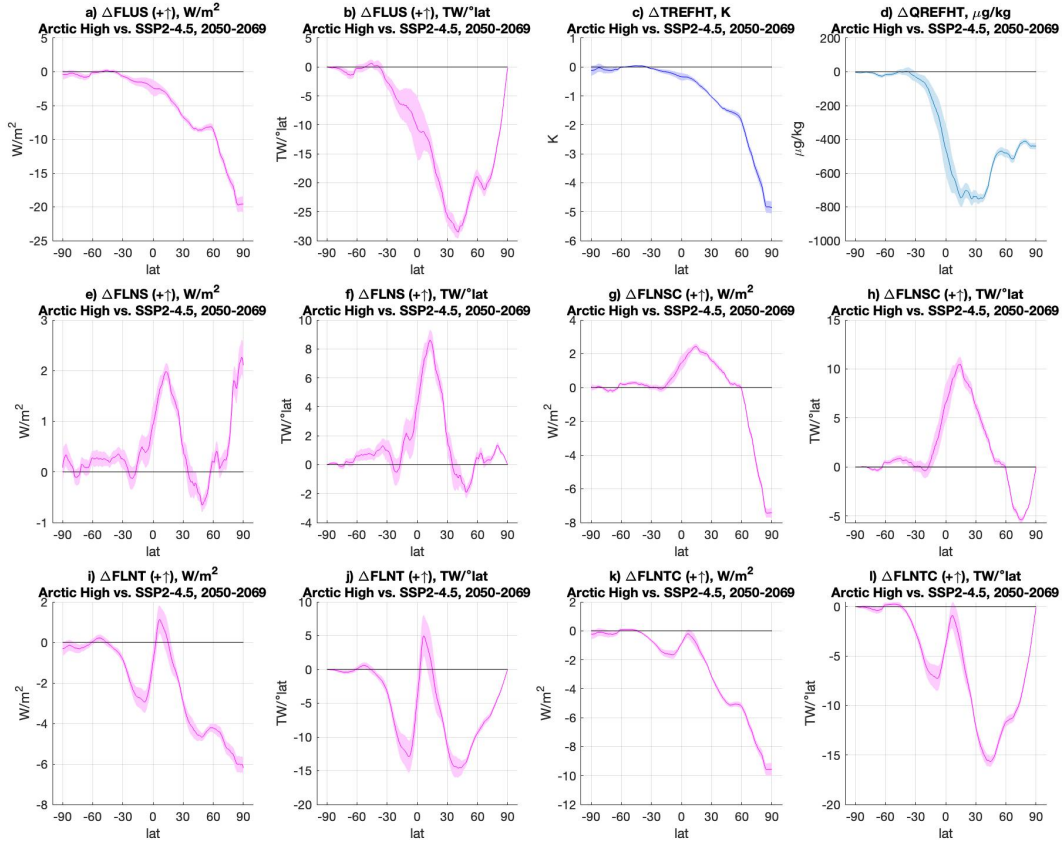


Figure 3. Changes to LW fluxes and near-surface temperature and humidity for Arctic High relative to SSP2-4.5, averaged over 2050-2069. The top row plots changes to upwelling LW at the surface (a, b) and near-surface temperature (c) and humidity (d); the middle row plots changes in net LW flux at the surface, and the bottom row plots changes in top-of-model net LW fluxes. All LW fluxes (positive up for all) are plotted in both W/m^2 (1st and 3rd columns) and in TW per degree latitude (2nd and 4th columns); the two left columns show "full-sky" fluxes with clouds, and the two right right columns show "clearsky" fluxes without clouds. All shading shows standard error as described in Text S2.

sphere (3d), which has implications for GrIS SMB (see Fig. 7 and accompanying discussion). Humidity reduction is largest near the tropics; comparing 3a-b with 3g-h, Arctic High actually increases upwelling surface LW in the tropics despite reduced emitted LW, indicating a reduction in trapped LW that correlates with the region of reduced near-surface humidity. Comparing full-sky (3e-f) and clear-sky (3g-h) net upwelling surface LW, the addition of clouds moves the change in forcing at high latitudes from negative to positive, indicating a strong reduction in LW trapped near the surface by clouds in the Arctic. The net effect of Arctic High on top-of-model outgoing LW radiation (OLR) is a reduction in OLR in the Arctic, the northern hemisphere mid-latitudes, and the southern hemisphere tropics and extratropics, and an increase in outgoing OLR in the northern hemisphere tropics (3i-j). The effect of the southward ITCZ shift on cloud cover is also visible, as the addition of clouds increases OLR in the northern hemisphere tropics and decreases OLR in the southern hemisphere tropics (compare 3i-j with 3k-l).

3.2 Arctic Impacts

The loss of Arctic sea ice has been shown to be reversible in climate models (Armour et al., 2011; Ridley et al., 2012); both globally-focused SAI (Jiang et al., 2019; W. Lee et al., 2020) and high-latitude SAI (Robock et al., 2008; Jackson et al., 2015; W. Lee et al., 2021) have been shown to increase sea ice extent. In Fig. 4, we present sea ice model output for the Arctic-focused SAI strategies against the globally-focused SAI strategies and Historical/SSP2-4.5. In 2035, at the start of the SAI simulations, September NH sea ice under SSP2-4.5 has an extent of 1.0 ± 0.1 million km^2 , and this decreases to 0.39 ± 0.03 million km^2 by the 2050-2069 period. Arctic High restores September NH sea ice extent to 4.8 ± 0.1 million km^2 during this period, slightly above the target for that simulation (4.45) and statistically identical to the Global+0.5 average (4.85 ± 0.06). Arctic Low restores NH September sea ice extent to 2.1 ± 0.1 million km^2 , also slightly above the target value (1.98) and indistinguishable from Global+1.5 (1.95 ± 0.06). Changes to the seasonal cycle of sea ice (Fig. 4) relative to the reference period (see Table 1 for reference periods) can also be observed: both Arctic High and Arctic Low have lower sea ice extent than their respective reference periods in the winter months, meaning that while the Arctic-focused SAI strategies restore September sea ice to or above their targets, they restore a smaller fraction of the lost winter sea ice. This may be due at least in part to the seasonality of the injection strategy, in which AOD (see Fig. 1c) and temperature changes (see Fig. 8b) are dominant in the summer; in contrast, all three global strategies, which inject year-round and primarily in the southern hemisphere, overcompensate winter sea ice extent relative to the reference period (this is a change from global strategies in CESM1(WACCM); Jiang et al. (2019) found that GLENS, which also used a global strategy but injected primarily in the northern hemisphere, overcompensated summer sea ice extent and undercompensated winter sea ice extent, the same pattern seen in Arctic High). However, the extent of sea ice is not only affected by SW radiation and temperature, but also other factors such as atmospheric and oceanic circulation (Moore et al., 2014), including dynamic effects of SAI-induced stratospheric heating (Jiang et al., 2019) and further study would be needed to investigate these influences. As discussed in Jiang et al. (2019), changes to the seasonal cycle have environmental and ecological implications; Dai et al. (2019) found that Arctic Amplification (AA) in response to sea ice loss mainly occurs in the cold season because winter surface waters are much warmer than sea ice and therefore emit more longwave (LW) radiation, and therefore undercompensating winter sea ice extent may affect the ability of Arctic-focused SAI to limit AA. Additionally, sea ice extent may influence the strength of the Atlantic Meridional Overturning Circulation (AMOC) via freshwater flux changes (Xie et al., 2022), and therefore changes to the seasonal cycle of sea ice may affect the seasonal cycle of the oceanic circulation.

In regions containing permafrost, the upper portion of the ground that thaws in the summer and re-freezes in the autumn is called the active layer. The maximum an-

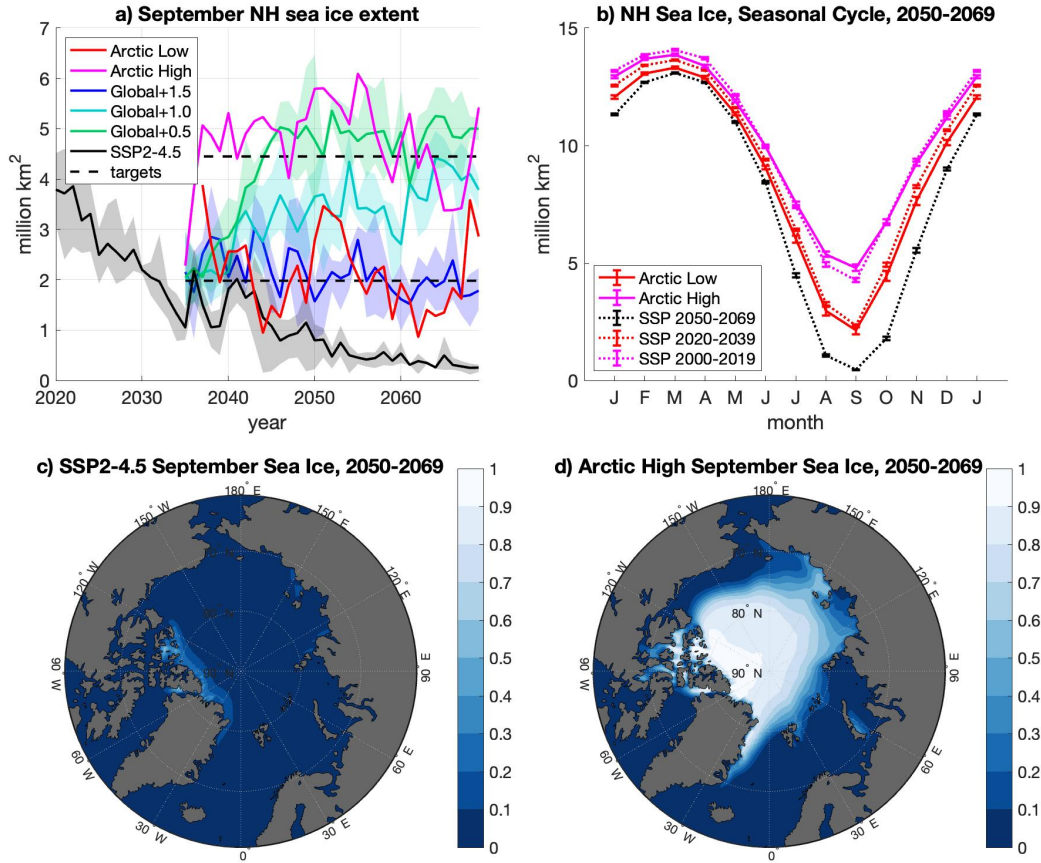


Figure 4. Northern Hemisphere (NH) sea ice extent. Panel (a) plots September NH sea ice extent as a function of time. Global and SSP2-4.5 data are ensemble means; shading denotes ensemble spread. Panel (b) compares seasonal cycles of NH sea ice extent for Arctic High and Arctic Low (averaged over 2050-2069) to their respective reference periods from Historical/SSP2-4.5 (see Table 1 for reference periods). Errorbars denote standard error as in Text S2. Dashed lines in panels (a) and (b) denote September sea ice targets for Arctic High and Arctic Low strategies. Panels (c) and (d) plot maps of September sea ice extent for SSP2-4.5 ensemble average and Arctic High, respectively, averaged over 2050-2069. The color scale denotes the fraction of each grid cell covered in sea ice.

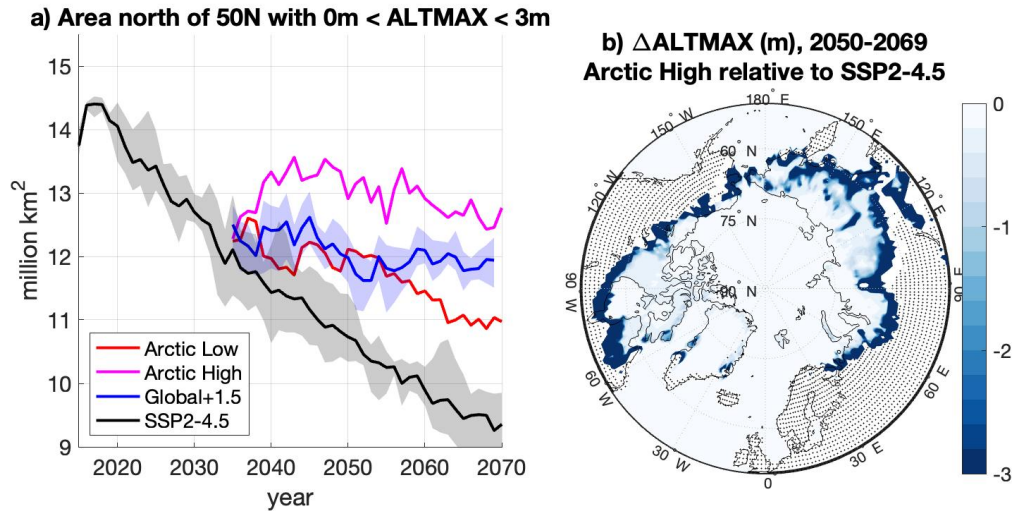


Figure 5. Annual maximum active layer thickness (ALTMAX). Panel (a) plots a timeseries of the area north of 50°N with ALTMAX between 0 and 3 meters; for Global+1.5 and SSP2-4.5, shading denotes ensemble spread. Panel (b) shows changes in ALTMAX for Arctic High relative to SSP2-4.5, averaged over the 2050-2069 period for both simulations. Hatching represents areas with no statistically detectable difference at the 95% confidence level according to the two-sample t-test. Light blue ($\Delta\text{ALTMAX} < 3\text{m}$) indicates a decrease in active layer thickness in permafrost and near-permafrost regions, whereas dark blue ($\Delta\text{ALTMAX} \geq 3\text{m}$) indicates increased permafrost area relative to SSP2-4.5.

nual depth of the active layer, called ALTMAX in CESM2, is commonly used to diagnose permafrost extent (e.g., Lawrence et al. (2015)); a small annual maximum active layer thickness (i.e., $\leq 3\text{m}$) is indicative that only the near-surface soil has become unfrozen during the past year, and there is permafrost underneath. In Fig. 5, we present permafrost diagnostics for our Arctic-focused strategies against Global+1.5 and SSP2-4.5. Panel (a) shows timeseries of near-surface permafrost extent. When SAI begins in 2035, the permafrost extent under SSP2-4.5 is 12.1 million km^2 , and the extent decreases to 9.96 ± 0.03 million km^2 by the 2050-2069 period. Arctic Low, Arctic High, and Global+1.5 all increase permafrost area relative to SSP2-4.5, but none of them restore permafrost to the extent of their respective reference periods: 11.46 ± 0.03 for Arctic Low and 11.88 ± 0.03 for Global+1.5 (compared to 12.70 ± 0.03 for SSP2-4.5 2020-2039), and 12.86 ± 0.06 for Arctic High (compared to 14.26 ± 0.03 for Historical/SSP2-4.5 2000-2019). A map of the changes for Arctic High is shown in panel (b); Arctic High both decreases ALTMAX in permafrost regions (light blue), which means a deeper column of soil remains frozen year-round, and increases permafrost area (dark blue). This expanded permafrost area reaches furthest to the south in northeastern Asia, but also spans the entire width of Russia and most of the width of North America. In contrast with sea ice, Global+1.5 increases permafrost area more than Arctic Low; this may be because Global+1.5 cools the mid-latitudes more effectively than Arctic Low (see Fig. 8c below), whereas September sea ice is mainly found north of 75°N, where these strategies provide comparable amounts of cooling.

In Fig. 6, we present land model carbon output for our Arctic-focused simulations and SSP2-4.5. Under SSP2-4.5, the Arctic ecosystem as a whole continues to take up carbon during the simulation period due to enhanced vegetation growth associated with CO_2 fertilization and due to a warmer and more hospitable climate for plants. Soil car-

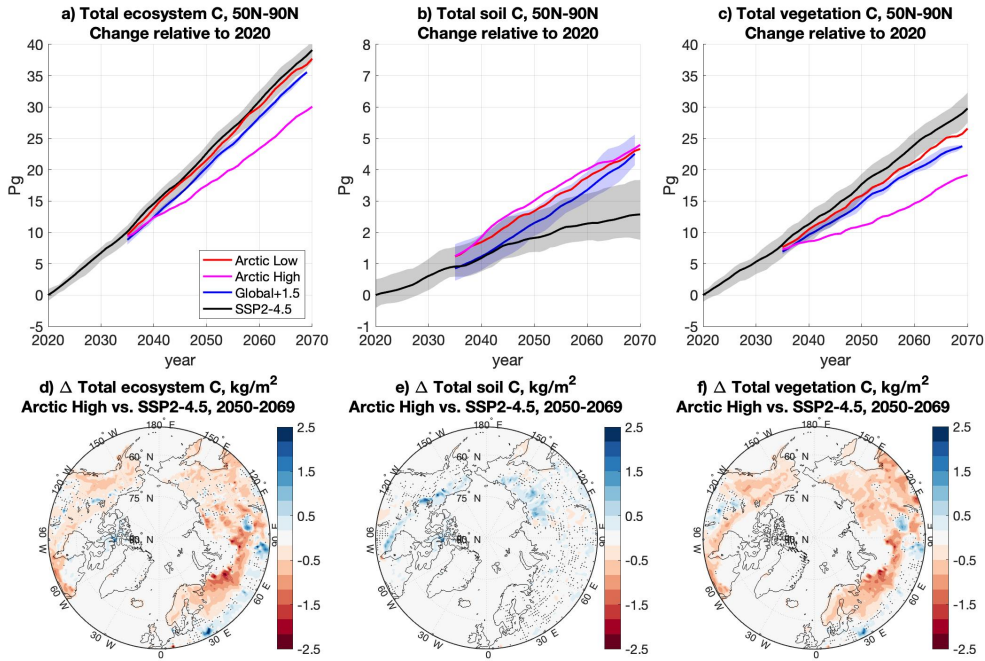


Figure 6. Carbon and carbon density. The top row plots timeseries of ecosystem (a), soil (b), and vegetation (c) carbon content relative to 2020 (note the different y-axis scaling for panel b); for SSP2-4.5, shading denotes ensemble standard error as described in Text S2 of the Supporting Information. The bottom row plots maps of changes in ecosystem (d), soil (e), and vegetation (f) carbon density in the 50°N-90°N region for Arctic High relative to SSP2-4.5, averaged over 2050-2069 for both simulations. Hatching represents areas with no statistically detectable difference at the 95% confidence level according to the two-sample t-test.

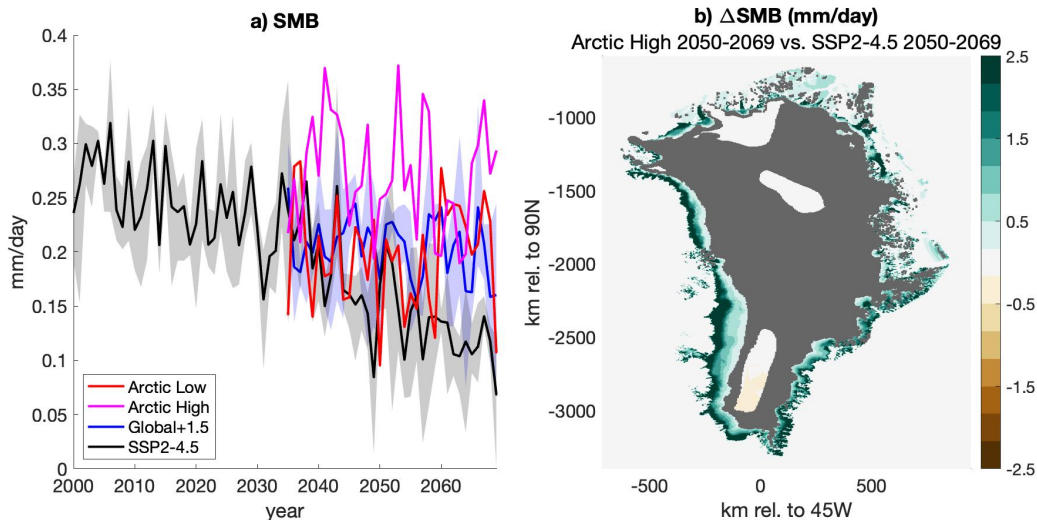


Figure 7. Changes in GrIS surface mass balance (SMB). Panel (a) plots annual mean SMB as a function of time; shading denotes ensemble spread. Panel (b) plots changes in SMB for Arctic High relative to SSP2-4.5 averaged over 2050-2069; shading denotes regions with no statistical change according to the two-sample t-test at a 95% significance level.

bon also increases in response to the enhanced litter and root carbon inputs near the surface, even though the permafrost thawing is leading to soil carbon losses due to enhanced decomposition at depth. In the Arctic SAI scenarios, the high-latitudes continue to be a sink of carbon as the plants respond positively to the increasing CO_2 . In Arctic High, the stronger cooling slows the rate of vegetation carbon gains, and also decreases permafrost soil carbon losses. The reduction in vegetation carbon gains is more impactful, which leads to the high-latitudes being a weaker carbon sink in Arctic High compared to Arctic Low and SSP2-4.5. For Arctic Low and Global+1.5, the changes to soil and vegetation carbon storage are the same signs as those of Arctic High, but the opposing effects are comparable in magnitude, and the overall effect is no significant difference in the total ecosystem carbon relative to SSP2-4.5 during the 2050-2069 period. This difference may be in part because Arctic High cools the mid-latitudes more efficiently than Arctic Low and Global+1.5 (Fig. 8c-d), but changes between 50° - 60° do not completely account for this nonlinearity. Inclusion of permafrost and other high-latitude climate-carbon feedbacks within ESMs like CESM is relatively new and remains highly uncertain; a recent intercomparison project of permafrost-enabled land models found a very large spread in response of both high-latitude soil and vegetation carbon stocks to projected climate change (McGuire et al., 2018). Therefore, the high-latitude carbon stock results presented here should be viewed with caution and treated as indicative only as representative of possible carbon budget consequences from SAI. Additionally, plants take up carbon in the form of CO_2 , whereas soil carbon can be released as both CO_2 and CH_4 , and so directly comparing carbon stocks does not fully quantify the effects of SAI on greenhouse gases in the atmosphere. Further development and validation of permafrost and carbon flux representation in Earth System models are needed to provide a foundation for more robust assessment of the impacts of SAI.

Surface mass balance (SMB) is the net change in mass at the surface of a glacier or ice sheet due to precipitation, evaporation, and runoff. Changes to SMB are likely responsible for an estimated 50-60% of the contribution of the GrIS to sea level rise over the past 30 years (van den Broeke et al., 2017; IMBIE, 2020). Globally-focused SAI has previously been found to increase GrIS SMB by reducing near-surface temperature and

humidity (Moore et al., 2019), which Arctic-focused SAI also reduces (see Fig. 3c-d and 8e; maps of these variables over Greenland are contained in Fig. S5 of the SI). In Fig. 7, we present changes to GrIS SMB for Arctic High relative to SSP2-4.5. When injection begins in 2035, GrIS SMB is approximately 0.24 mm/day; in the SSP2-4.5 scenario, this value decreases to 0.132 ± 0.006 mm/day by the 2050-2069 period. The Arctic Low strategy increases this value to 0.19 ± 0.01 mm/day, statistically indistinguishable from Global+1.5 during the same period (0.198 ± 0.006) and slightly lower than SSP2-4.5 during the Arctic Low reference period (see 1 for reference periods) of 2020-2039 (0.229 ± 0.007). Arctic High further increases SMB to 0.27 ± 0.01 during the 2050-2069 period, slightly lower than its respective reference period of 2000-2019 (0.258 ± 0.007). In these simulations, changes to SMB appear to be dominated by decreases in runoff (maps of runoff and other components for SMB are contained in Fig. S5), especially in the western ablation zone, which is consistent with the results of Moore et al. (2019) for globally-focused SAI. Although CESM2(WACCM) accounts for many important dynamic and thermodynamic processes governing surface mass balance, changes in ice dynamics processes such as glacial calving are not considered, so the ice sheet geometry is fixed with time. The relatively short duration of the simulations means that dynamic responses to ice sheet geometrical changes imposed by changing SMB are likely to be insignificant (Slater et al., 2019), but changes in ice elevation would contribute enhanced ablation as the surface lowers; this would likely be on the order of 10% for SSP2-4.5, while being less important for the SAI scenarios (Moore et al., 2019). Further work is necessary to determine the effects of high-latitude SAI relative to global strategies on glacial calving and other dynamic processes.

3.3 Global Impacts

In Fig. 8, we present surface temperature output from our simulations. As expected, Arctic High produces less global cooling than Global+1.5 despite injecting slightly more; averaged over the 2050-2069 period, Arctic Low provides roughly $1/4^\circ\text{C}$ of cooling (0.041 ± 0.005 K/Tg), Arctic High provides $2/3^\circ\text{C}$ of cooling (0.062 ± 0.004 K/Tg), and Global+1.5 provides close to 1°C of cooling (0.102 ± 0.002 K/Tg). However, in the 60°N - 90°N region, the Arctic-focused strategies provide more cooling per unit injection than Global+1.5 (0.26 ± 0.02 K/Tg for Arctic Low, 0.29 ± 0.01 K/Tg for Arctic High, and 0.207 ± 0.009 K/Tg for Global+1.5). It is noteworthy that Arctic High provides more global cooling per unit injection than Arctic Low, as strategies with higher injection rates generally cool less efficiently due to the physics of aerosol coagulation (Vioni et al., 2020; Pierce et al., 2010; Niemeier et al., 2011). The two Arctic-focused strategies provide similar rates of high-latitude cooling per unit injection; the difference in global cooling efficiency comes from more efficient cooling by Arctic High at low and mid-latitudes in the Northern Hemisphere (Fig. 8d). The different distributions of cooling by different strategies have implications for how they affect the high-latitude climate. Global+1.5 and Arctic Low have similar rates of September sea ice recovery (Fig. 4a), and this may be because they provide similar cooling at very high latitudes where sea ice is present. However, Global+1.5 cools the middle latitudes, where large areas of permafrost or potential permafrost are located, more than Arctic Low, and permafrost recovery under Global+1.5 is higher than for Arctic Low (Fig. 5a).

The detectable cooling from Arctic High covers most of the Northern Hemisphere, but very little cooling extends into the Southern Hemisphere; the cooling seen near Antarctica in Fig. 8e is likely due to natural variability, but it is possible that dynamical changes may also be responsible. As shown in panel 8b, the largest cooling effect at high latitudes from Arctic High occurs not during the period of maximum AOD in the early summer (see Fig. 1c) but rather in the autumn; this suggests that the cooling at the highest latitudes is due at least in part to the higher albedo of the increased sea ice extent in the autumn (see Fig. 4b). For Arctic High, much of the surface temperature between 45°N - 90°N is indistinguishable from the reference period of 2000-2019 (see Table 1 for refer-

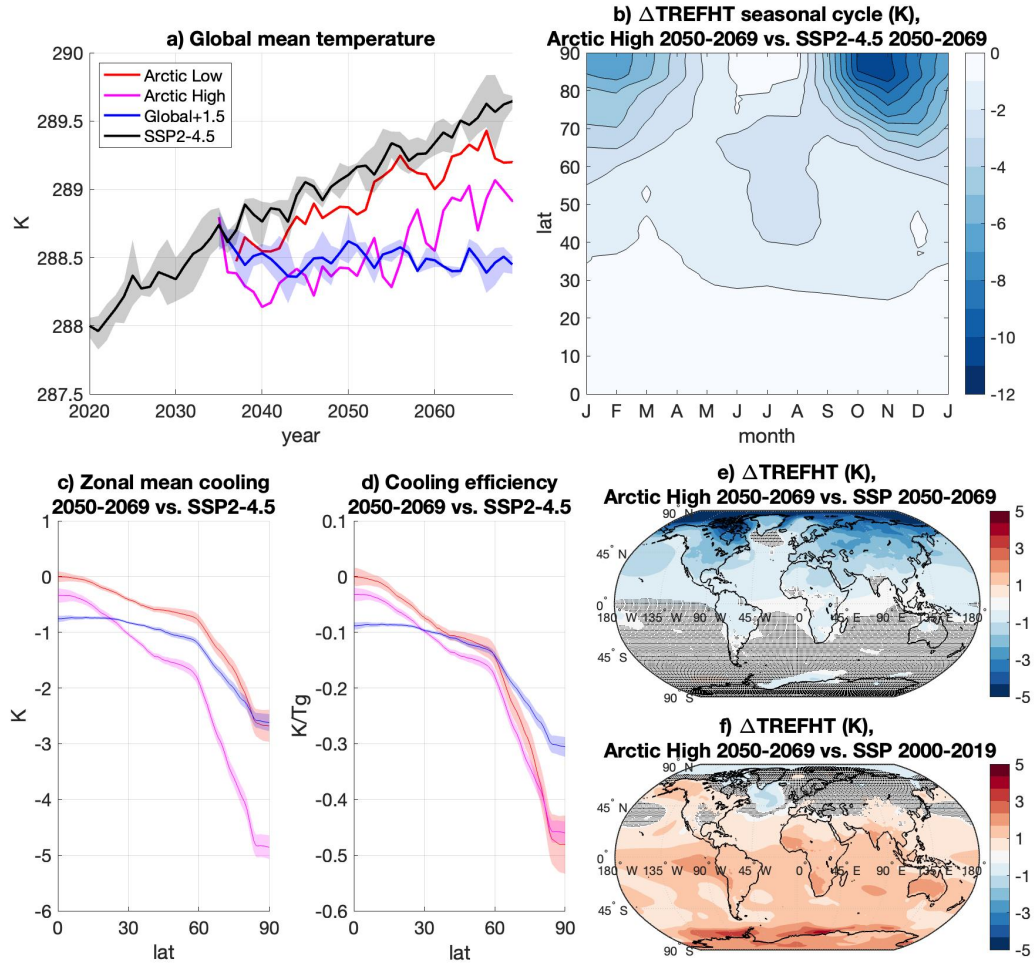


Figure 8. Surface temperature. Panel (a) plots globally averaged, annual mean surface temperature as a function of time; shading denotes ensemble spread. Panel (b) plots changes to the seasonal cycle of zonal mean temperature for Arctic High (2050-2069 average) relative to SSP2-4.5 during the same period. Panels (c) and (d) plot zonal mean cooling and zonal mean cooling per unit injection rate, respectively; cooling is relative to SSP2-4.5 averaged over the 2050-2069 period, and shading denotes standard error as described in Text S2. Panels (e) and (f) plot maps of surface temperature changes for Arctic High (2050-2069 average) relative to SSP2-4.5 (2050-2069 average and 2000-2019 average, respectively). Shading represents changes that are not statistically significant according to the two-sample t-test at the 95% confidence level.

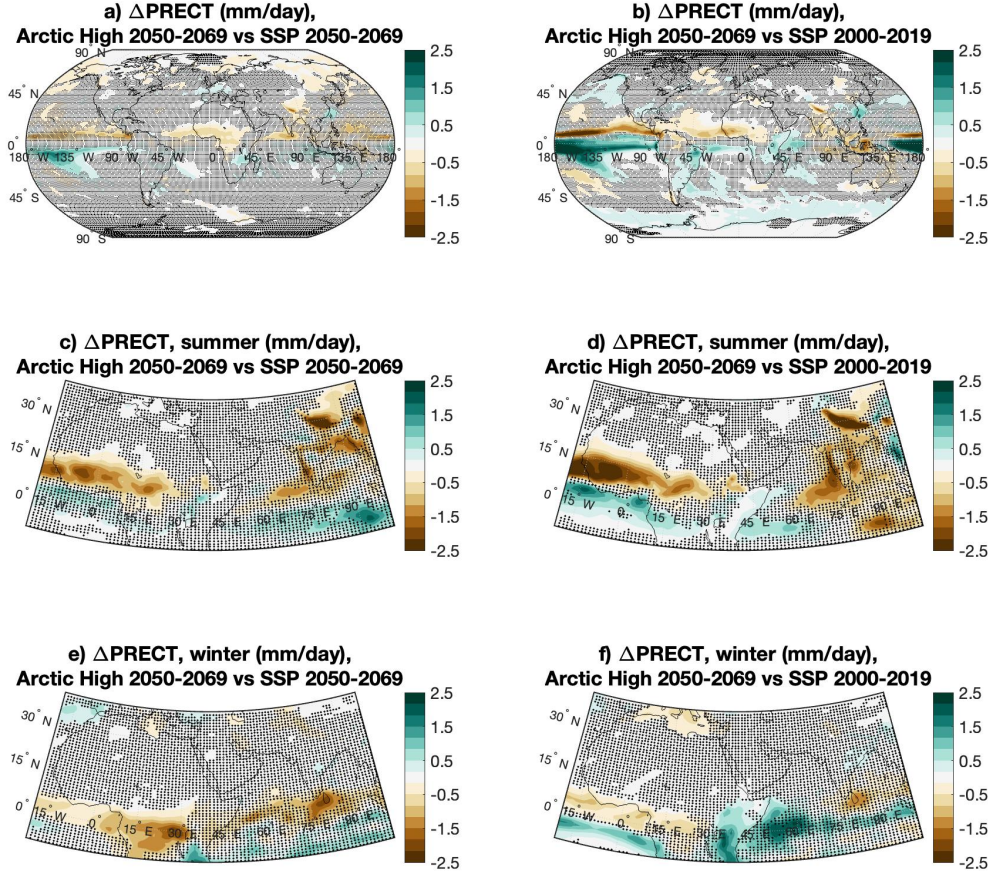


Figure 9. Precipitation, Arctic High 2050-2069 relative to SSP2-4.5 2050-2069 (left column) and Historical/SSP2-4.5 2000-2019 (right column). The top row shows changes to annual mean precipitation; the middle and bottom rows show changes to summer (JJA) and winter (DJF) precipitation over India and northern Africa, respectively. Shading indicates no statistically significant change at the 95% confidence level using the two-sample t-test.

ence periods) in the SSP2-4.5 scenario, but some spatial and temporal differences are present. For instance, the northeastern Pacific is warmer and the northern Atlantic is cooler under the Arctic High strategy than during the reference period, a response also seen in the temperature response of the globally-focused simulations of Richter et al. (2022). This is likely due at least in part to the behavior of the Atlantic Meridional Overturning Circulation (AMOC); in CESM1, AMOC weakened under global warming but accelerated under GLENS, leaving a similar persistent warming in the north Atlantic (Fasullo et al., 2018). In CESM2(WACCM), the effects of globally-focused SAI on AMOC have the same sign but a smaller magnitude, reducing the weakening but not reversing it (Tilmes et al., 2020). The effects of Arctic-focused SAI are similar: the strength of the AMOC under SSP2-4.5 is 23.7 ± 0.1 Svd in 2000-2019 and decreases to 17.2 ± 0.2 Svd in 2050-2069, but only decreases to 19.1 ± 0.2 Svd under Arctic Low and 21.1 ± 0.2 Svd under Arctic High (see Fig. S3 for a plot of AMOC behavior).

In Fig. 9, we present precipitation for Arctic High (2050-2069) relative to SSP2-4.5 during the same period and during the 2000-2019 reference period (see Table 1 for reference periods). Under global warming, the warmer atmosphere has a greater capacity to carry water; in the Historical and SSP2-4.5 simulations, global mean precipitation increases from 4.097 ± 0.008 mm/day in 2000-2019 to 4.263 ± 0.007 mm/day in 2050-2069. The cooling provided by SAI offsets this change; for Arctic Low (4.25 ± 0.01 mm/day in 2050-2069), this reduction is indistinguishable from SSP2-4.5, but for Arctic High (4.20 ± 0.02 mm/day), the reduction is detectable. As expected, high-latitude SAI pushes the ITCZ southward (Haywood et al., 2013; W. Lee et al., 2020), and this southward shift in tropical precipitation is clearly visible in Fig. 9. For SSP2-4.5, the 2050-2069 ITCZ location as measured by the centroid of tropical precipitation between 20°S and 20°N (Donohoe et al., 2013; Frierson & Hwang, 2012; W. Lee et al., 2020) is $1.07^{\circ}\text{N} \pm 0.05^{\circ}$. During the same period, Arctic Low pushes the ITCZ southward to $0.8^{\circ}\text{N} \pm 0.1^{\circ}$, and Arctic High to $0.54^{\circ}\text{N} \pm 0.08^{\circ}$. Such a southward shift of the ITCZ could have consequences for people who rely on tropical precipitation patterns such as the African monsoon (Haywood et al., 2013; Krishnamohan & Bala, 2022); Robock et al. (2008) reported disruption to the Indian monsoon from 3 Tg/yr high-latitude injection, and similar changes are clearly visible here relative to SSP2-4.5 (Fig. 9c,e) and even more so relative to the reference period (Fig. 9d,f). Globally-focused strategies commonly inject in both hemispheres with the goal of avoiding such a result (Kravitz et al., 2017; MacMartin et al., 2022; Richter et al., 2022), and combining Arctic-focused SAI with injection in the Southern Hemisphere (either Antarctic or tropical) could reduce the risk of a change in the ITCZ. We note that climate models disagree on the expected sign of future ITCZ change due to global warming and changes to anthropogenic aerosols (Byrne et al., 2018), and should the ITCZ shift northward, a southward shift in the ITCZ could be a goal of Arctic-focused SAI rather than an unwanted outcome; regardless, given the importance of tropical precipitation, the effects of SAI on the location of the ITCZ should remain a forefront concern for any future discussion of Arctic-focused SAI. Other possible influences to tropical precipitation also require further exploration; the latitudinal extent of the Hadley and Walker cells is expected to change in future GHG climates (Vallis et al., 2015), and the descending limbs of the Hadley circulation are associated with deserts. SAI tends to reverse these impacts (Guo et al., 2018), although the situation is complicated by stratospheric heating (Cheng et al., 2022).

In the Historical and SSP2-4.5 scenarios, sulfur pollution peaks in the late 1900s and decreases throughout the 21st century, averaging 21.69 ± 0.05 Tg/yr during the 2050-2069 period, including 14.62 ± 0.05 Tg/yr in the northern hemisphere. During this period, Arctic Low and Arctic High inject 5.57 Tg/yr and 10.66 Tg/yr of SO_2 , or (dividing by molar weights) approximately 2.8 and 5.3 Tg/yr of sulfur (representing approximately 25% and 50% global increases), respectively. In Fig. 10, we present 2050-2069 changes to sulfur deposition from SO_4 for Arctic High relative to one ensemble member of SSP2-4.5 (SO_4 deposition model output was not saved for the second and third SSP2-4.5 ensemble members). The bulk of the increased sulfur deposition (Fig. 10a) is concentrated in the late summer between 45°N - 60°N , although increased deposition is present throughout 30°N - 60°N in all months of the year. The location of the maximum increase in annual mean sulfur deposition (Fig. 10b) correlates to the region of largest increase in atmospheric sulfur burden seen in Fig. 2j. Relative to SSP2-4.5, sulfur deposition in the 30°N - 60°N latitude band increases from 5.19 ± 0.04 Tg/yr to 8.38 ± 0.09 Tg/yr, an increase of 60%; the increased deposition is comparable to Historical/SSP2-4.5 during the 2010-2029 period (Fig. 10b, dark blue dotted line), approximately 40 years earlier. While the absolute increase at high latitudes is smaller, the baseline deposition is also smaller, meaning that the relative increase in sulfur pollution is large. Pollution from mid latitudes has long been observed in the Arctic regions (Arctic Haze; Yang et al. (2018)) and is seasonally concentrated in the spring and composed primarily of sulfate aerosols, causing lake acidification during spring thaw. Arctic High increases the deposition north of 60°N from 0.63 ± 0.01 Tg/yr to 1.47 ± 0.02 Tg/yr, an increase of 133%. This increased

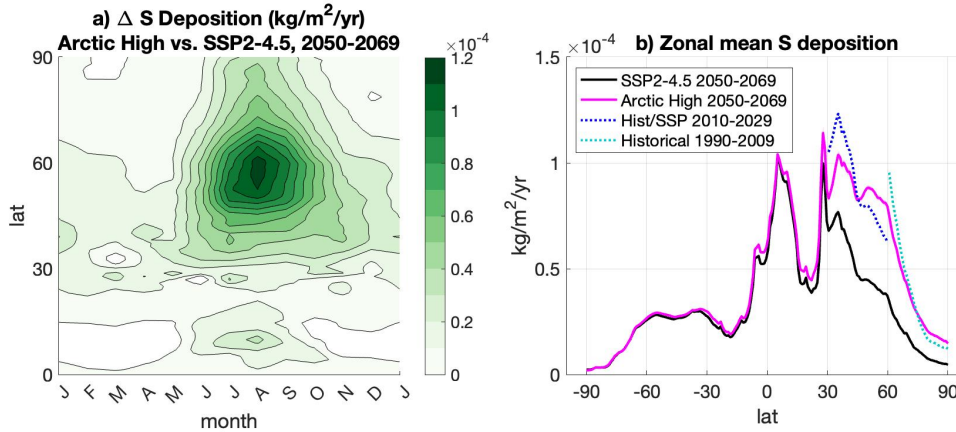


Figure 10. Changes to zonal mean sulfur deposition. Panel (a) displays the seasonal cycle of zonal mean sulfur deposition in $\text{kg}/\text{m}^2/\text{yr}$ for Arctic High 2050-2069 relative to SSP2-4.5 2050-2069. Panel (b) shows zonal mean sulfur deposition for Arctic High and SSP2-4.5, both averaged over 2050-2069; shading denotes standard error as described in Text S2. Included for comparison are mid-latitude and high-latitude sulfur deposition for Historical/SSP2-4.5 in the 2010-2029 and 1990-2009 periods, respectively, which are similar to the increased deposition under Arctic High; these are indicated by dotted lines. (Note: sulfur deposition data for Historical/SSP2-4.5 is taken from runs using the full-atmosphere (TSMLT) configuration of WACCM (one ensemble member) instead of the MA configuration because deposition output was not saved for the -MA simulations; emissions are the same for both configuration and tropospheric lifetime is short, so deposition should be similar).

deposition is comparable to Historical during the 1990-2009 period (Fig. 10b, light blue dotted line), approximately 60 years earlier. Both the large absolute increase in the mid-latitudes and the large relative change at high latitudes would likely impact ecosystems and the people who live in these regions, and further study of the implications of increased sulfur deposition in these areas is necessary.

4 Conclusions and Discussion

Both Arctic-focused strategies restored and maintained September sea ice to within 10% of their targets, demonstrating that Arctic-focused SAI can reverse the loss of sea ice and that higher injection rates lead to greater restoration of sea ice. The results also show that Arctic-focused SAI could mitigate other high-latitude impacts of global warming: permafrost extent is higher relative to SSP2-4.5 under both strategies, and both strategies increased GrIS SMB by reducing runoff. Arctic Low and Arctic High cool the Arctic and increase September sea ice extent more efficiently than Global+1.5; this is in contrast to Robock et al. (2008), in which 5 Tg/yr of equatorial injection cooled the high latitudes and restored September sea ice much more effectively than 3 Tg/yr of injection at 68°N. However, the difference also reflects evolution of the injection strategies, as Global+1.5 injected at multiple tropical and near-tropical locations (instead of just the equator) and Arctic Low and Arctic High injected in spring (instead of year-round). The Arctic-focused strategies also increase GrIS SMB more efficiently than Global+1.5. However, the Arctic-focused strategies and Global+1.5 all provide comparable amounts of cooling per unit injection in the mid-latitude and extrapolar regions (Arctic High is slightly more efficient in this region) and have comparable rates of permafrost area in-

crease, indicating that tropical and Arctic injection may be comparably effective for mid-latitude impacts. Arctic-focused SAI also introduces other high-latitude effects, including changes to the seasonal cycle of high-latitude temperature and sea ice. Arctic High increases high-latitude sulfur deposition by more than double, equivalent to a backwards step of approximately 60 years for sulfur deposition rates in the Arctic. Lastly, in this model, Arctic High slows overall carbon uptake by the Arctic ecosystem via reduced storage in vegetation. While permafrost modeling is highly uncertain, this demonstrates how in this model, global warming produces a negative feedback by increasing plant uptake of CO₂ at high latitudes, and an intervention that reduces that warming could also dampen that feedback.

It was originally hypothesized that the effects of high-latitude injection could be largely confined to the Arctic due to the poleward direction of the stratospheric Brewer-Dobson circulation (Lane et al., 2007). However, Robock et al. (2008) concluded this was not the case, citing substantial impacts outside of the Arctic, including reductions to downward surface SW well south of the injection site and changes to tropical precipitation. We reach a similar conclusion; while surface cooling is highest at the pole for Arctic-focused SAI, Arctic High causes detectable cooling nearly everywhere in the northern hemisphere. Although sulfur mixing ratio and AOD are highest near the pole, zonally-integrated sulfur burden and reduction in top-of-model incoming SW energy peak south of the injection location, and Arctic High increases sulfur deposition in the mid-latitudes by 60%. The hemispherically asymmetric forcing causes a substantial southward shift in the ITCZ and disrupts the seasonal monsoons. This shift could be offset by combining Arctic-focused injection with injection in the southern hemisphere, either in the tropics or at the Antarctic. Similar studies in other models would greatly help to reduce uncertainty, including the quantification of both how Arctic-focused and globally-focused SAI impact the Arctic and also how Arctic-focused SAI impacts regions outside the Arctic (and how southern hemisphere injection might offset this). Simulations that include an evolving ice sheet would be especially useful in determining the effects of Arctic SAI on ice dynamics, and longer simulations would be useful in determining the effects of SAI on natural variability. Additionally, there is ample room for further in-depth exploration of SAI effects, such as changes to the circulation or analysis of the various radiative, humidity, and temperature feedbacks that govern Arctic amplification.

5 Open Research

Data used in this study is available through the Cornell eCommons repository at <https://doi.org/10.7298/gnmp-q653>. Additional data from the Global+1.5, Global+1.0, and Global+0.5 simulations can be likewise be found through the Cornell eCommons repository at Visioni (2022), <https://doi.org/10.7298/xr82-sv86>.

Acknowledgments

The authors would like to thank attendees of the 2022 Gordon Research Seminar and Gordon Research Conference for Climate Engineering, who offered feedback on this project that substantially improved the quality of our manuscript. The authors would also like to acknowledge high-performance computing support from Cheyenne (<https://doi.org/10.5065/D6RX99HX>) provided by NCAR's Computational and Information Systems Laboratory, sponsored by the National Science Foundation. Support for WL and DM was provided by the National Science Foundation through agreement CBET-1818759. Support for DV was provided by the Atkinson Center for a Sustainable Future at Cornell University. Support for BK was provided in part by the National Sciences Foundation through agreement CBET-1931641, the Indiana University Environmental Resilience Institute, and the Prepared for Environmental Change Grand Challenge initiative. The Pacific Northwest National Laboratory is operated for the U.S. Department of Energy by Battelle Memorial Institute under contract DE-AC05-76RL01830. The CESM project is supported primar-

ily by the National Science Foundation. This work was supported by the National Center for Atmospheric Research, which is a major facility sponsored by the National Science Foundation under Cooperative Agreement No. 1852977, and by SilverLining through its Safe Climate Research Initiative.

References

- Armour, K. C., Eisenman, I., Blanchard-Wrigglesworth, E., McCusker, K. E., & Bitz, C. M. (2011). The reversibility of sea ice loss in a state-of-the-art climate model. *Geophysical Research Letters*, *38*(16). doi: <https://doi.org/10.1029/2011GL048739>
- Bamber, J. L., Westaway, R. M., Marzeion, B., & Wouters, B. (2018). The land ice contribution to sea level during the satellite era. *Environmental Research Letters*, *13*. doi: [10.1088/1748-9326/aac2f0](https://doi.org/10.1088/1748-9326/aac2f0)
- Biskaborn, B. K., Smith, S. L., Noetzli, J., Matthes, H., Vieira, G., Streletskiy, D. A., . . . Lantuit, H. (2019). Permafrost is warming at a global scale. *Nature Communications*, *10*. doi: [0.1038/s41467-018-08240-4](https://doi.org/10.1038/s41467-018-08240-4)
- Byrne, M. P., Pendergrass, A. G., Rapp, A. D., & Wodzicki, K. R. (2018). Response of the Intertropical Convergence Zone to Climate Change: Location, Width, and Strength. *Current Climate Change Reports*, *4*, 355–370. doi: <https://doi.org/10.1007/s40641-018-0110-5>
- Chen, Y., Liu, A., & Moore, J. C. (2020). Mitigation of Arctic permafrost carbon loss through stratospheric aerosol geoengineering. *Nature Communications*, *11*(2430). doi: <https://doi.org/10.1038/s41467-020-16357-8>
- Cheng, W., MacMartin, D. G., Kravitz, B., Visioni, D., Bednarz, E. M., Xu, Y., . . . Deng, X. (2022). Changes in Hadley circulation and intertropical convergence zone under strategic stratospheric aerosol geoengineering. *npj Climate and Atmospheric Science*, *5*(32). doi: [10.1038/s41612-022-00254-6](https://doi.org/10.1038/s41612-022-00254-6)
- Dai, A., Luo, D., Song, M., & Liu, J. (2019). Arctic amplification is caused by sea-ice loss under increasing CO₂. *Nature Communications*, *10*(121). doi: [0.1038/s41467-018-07954-9](https://doi.org/10.1038/s41467-018-07954-9)
- Danabasoglu, G., Bates, S. C., Briegleb, B. P., Jayne, S. R., Jochum, M., Large, W. G., . . . Yeager, S. G. (2012). The CCSM4 Ocean Component. *Journal of Climate*, *25*(5), 1361 – 1389. doi: [10.1175/JCLI-D-11-00091.1](https://doi.org/10.1175/JCLI-D-11-00091.1)
- Danabasoglu, G., Lamarque, J.-F., Bacmeister, J., Bailey, D. A., DuVivier, A. K., Edwards, J., . . . Strand, W. G. (2020). The community earth system model version 2 (cesm2). *Journal of Advances in Modeling Earth Systems*, *12*(2), e2019MS001916. doi: <https://doi.org/10.1029/2019MS001916>
- Donohoe, A., Marshall, J., Ferreira, D., & Mcgee, D. (2013, 05). The Relationship between ITCZ Location and Cross-Equatorial Atmospheric Heat Transport: From the Seasonal Cycle to the Last Glacial Maximum. *Journal of Climate*, *26*(11), 3597-3618. doi: [10.1175/JCLI-D-12-00467.1](https://doi.org/10.1175/JCLI-D-12-00467.1)
- DuVivier, A. K., Holland, M. M., Kay, J. E., Tilmes, S., Gettelman, A., & Bailey, D. A. (2020). Arctic and antarctic sea ice mean state in the community earth system model version 2 and the influence of atmospheric chemistry. *Journal of Geophysical Research: Oceans*, *125*(8), e2019JC015934. doi: <https://doi.org/10.1029/2019JC015934>
- England, M. R., Eisenman, I., Lutsko, N. J., & Wagner, T. J. W. (2021). The recent emergence of arctic amplification. *Geophysical Research Letters*, *48*(15), e2021GL094086. (e2021GL094086 2021GL094086) doi: <https://doi.org/10.1029/2021GL094086>
- Fasullo, J. T., Tilmes, S., Richter, J. H., Kravitz, B., MacMartin, D. G., Mills, M. J., & Simpson, I. R. (2018). Persistent polar ocean warming in a strategically geoengineered climate. *Nature Geoscience*, *11*, 910–914. doi: <https://doi.org/10.1038/s41561-018-0249-7>
- Fox-Kemper, B., Hewitt, H., Xiao, C., Adalgeirsdottir, G., Drijfhout, S., Edwards, T., . . . Yu, Y. (2021). Ocean, cryosphere and sea level change. In V. Masson-Delmotte et al. (Eds.), *Climate change 2021: The physical science basis. contribution of working group I to the sixth assessment report of the intergovernmental panel on climate change* (pp. 1211–1362). Cambridge University Press.

- Frierson, D. M. W., & Hwang, Y.-T. (2012, 01). Extratropical Influence on ITCZ Shifts in Slab Ocean Simulations of Global Warming. *Journal of Climate*, 25(2), 720-733. doi: 10.1175/JCLI-D-11-00116.1
- Gettelman, A., Mills, M. J., Kinnison, D. E., Garcia, R. R., Smith, A. K., Marsh, D. R., ... Randel, W. J. (2019). The whole atmosphere community climate model version 6 (waccm6). *Journal of Geophysical Research: Atmospheres*, 124(23), 12380-12403. doi: <https://doi.org/10.1029/2019JD030943>
- Guo, A., Moore, J. C., & Ji, D. (2018). Tropical atmospheric circulation response to the g1 sunshade geoengineering radiative forcing experiment. *Atmospheric Chemistry and Physics*, 18(12), 8689-8706. doi: 10.5194/acp-18-8689-2018
- Haywood, J. M., Jones, A., Bellouin, N., & Stephenson, D. (2013). Asymmetric forcing from stratospheric aerosols impacts Sahelian rainfall. *Nature Climate Change*, 3, 660-665. (doi:10.1038/nclimate1857) doi: 10.1038/nclimate1857
- Hugelius, G., Strauss, J., Zubrzycki, S., Harden, J. W., Schuur, E. A. G., Ping, C.-L., ... Kuhry, P. (2014). Estimated stocks of circumpolar permafrost carbon with quantified uncertainty ranges and identified data gaps. *Biogeosciences*, 11(23), 6573-6593. doi: 10.5194/bg-11-6573-2014
- Hunke, E. C., Lipscomb, W. H., Turner, A. K., Jeffery, N., & Elliott, S. (2015). Cice: The los alamos sea ice model. documentation and software user's manual (5.1 ed.) [Computer software manual].
- IMBIE. (2020). Mass balance of the greenland ice sheet from 1992 to 2018. *Nature*, 579, 233-239. doi: 10.1038/s41586-019-1855-2
- Jackson, L. S., Crook, J. A., Jarvis, A., Leedal, D., Ridgwell, A., Vaughan, N., & Forster, P. M. (2015). Assessing the controllability of Arctic sea ice extent by sulfate aerosol geoengineering. *Geophysical Research Letters*, 42(4), 1223-1231. doi: 10.1002/2014GL062240
- Jiang, J., Cao, L., MacMartin, D. G., Simpson, I. R., Kravitz, B., Cheng, W., ... Mills, M. J. (2019). Stratospheric Sulfate Aerosol Geoengineering Could Alter the High-Latitude Seasonal Cycle. *Geophysical Research Letters*, 46(23), 14153-14163. doi: 10.1029/2019GL085758
- Kravitz, B., MacMartin, D. G., Mills, M. J., Richter, J. H., Tilmes, S., Lamarque, J.-F., ... Vitt, F. (2017). First Simulations of Designing Stratospheric Sulfate Aerosol Geoengineering to Meet Multiple Simultaneous Climate Objectives. *Journal of Geophysical Research: Atmospheres*, 122(23), 12,616-12,634. doi: 10.1002/2017JD026874
- Krishnamohan, K. S., & Bala, G. (2022). Sensitivity of tropical monsoon precipitation to the latitude of stratospheric aerosol injections. *Climate Dynamics*(59), 151-168. doi: 10.1007/s00382-021-06121-z
- Lane, L., Caldeira, K., Chatfield, R., & Langhoff, S. (Eds.). (2007). *Workshop report on managing solar radiation* (Vol. NASA/CP-2007-214558). NASA. Retrieved from <https://ntrs.nasa.gov/citations/20070031204>
- Lawrence, D. M., Fisher, R. A., Koven, C. D., Oleson, K. W., Swenson, S. C., Bonan, G., ... Zeng, X. (2019). The community land model version 5: Description of new features, benchmarking, and impact of forcing uncertainty. *Journal of Advances in Modeling Earth Systems*, 11(12), 4245-4287. doi: <https://doi.org/10.1029/2018MS001583>
- Lawrence, D. M., Koven, C. D., Swenson, S. C., Riley, W. J., & Slater, A. G. (2015). Permafrost thaw and resulting soil moisture changes regulate projected high-latitude co2 and ch4 emissions. *Environmental Research Letters*, 10(9). doi: 10.1088/1748-9326/10/9/094011
- Lee, H., Ekici, A., Tjiputra, J., Muri, H., Chadburn, S. E., Lawrence, D. M., & Schwinger, J. (2019). The response of permafrost and high-latitude ecosystems under large-scale stratospheric aerosol injection and its termination. *Earth's Future*, 7(6), 605-614. doi: <https://doi.org/10.1029/2018EF001146>
- Lee, W., MacMartin, D., Visoni, D., & Kravitz, B. (2020). Expanding the design

- space of stratospheric aerosol geoengineering to include precipitation-based objectives and explore trade-offs. *Earth System Dynamics*, *11*(4), 1051–1072. doi: 10.5194/esd-11-1051-2020
- Lee, W., MacMartin, D., Visioni, D., & Kravitz, B. (2021). High-Latitude Stratospheric Aerosol Geoengineering Can Be More Effective if Injection Is Limited to Spring. *Geophysical Research Letters*, *48*(9). doi: 10.1029/2021GL092696
- Lipscomb, W. H., Price, S. F., Hoffman, M. J., Leguy, G. R., Bennett, A. R., Bradley, S. L., ... Worley, P. H. (2019). Description and evaluation of the community ice sheet model (cism) v2.1. *Geoscientific Model Development*, *12*(1), 387–424. doi: 10.5194/gmd-12-387-2019
- Liu, X., Ma, P.-L., Wang, H., Tilmes, S., Singh, B., Easter, R. C., ... Rasch, P. J. (2016). Description and evaluation of a new four-mode version of the modal aerosol module (mam4) within version 5.3 of the community atmosphere model. *Geoscientific Model Development*, *9*(2), 505–522. doi: 10.5194/gmd-9-505-2016
- MacMartin, D. G., & Kravitz, B. (2019). The Engineering of Climate Engineering. *Annual Review of Control, Robotics, and Autonomous Systems*, *2*(1), 445–467. doi: 10.1146/annurev-control-053018-023725
- MacMartin, D. G., Kravitz, B., Keith, D. W., & Jarvis, A. (2014). Dynamics of the coupled human-climate system resulting from closed-loop control of solar geoengineering. *Climate Dynamics*, *43*(1-2), 243–258. doi: 10.1007/s00382-013-1822-9
- MacMartin, D. G., Visioni, D., Kravitz, B., Richter, J. H., Felgenhauer, T., Lee, W. R., ... Sugiyama, M. (2022). Scenarios for modeling solar radiation modification. *Proceedings of the National Academy of Sciences of the United States of America*.
- McGuire, A. D., Lawrence, D. M., Koven, C., Clein, J. S., Burke, E., Chen, G., ... Zhuang, Q. (2018). Dependence of the evolution of carbon dynamics in the northern permafrost region on the trajectory of climate change. *Proceedings of the National Academy of Sciences*, *115*(15), 3882–3887. doi: 10.1073/pnas.1719903115
- Mills, M. J., Richter, J. H., Tilmes, S., Kravitz, B., MacMartin, D. G., Glanville, A. A., ... Kinnison, D. E. (2017). Radiative and Chemical Response to Interactive Stratospheric Sulfate Aerosols in Fully Coupled CESM1(WACCM). *Journal of Geophysical Research: Atmospheres*, *122*(23), 13,061–13,078. doi: 10.1002/2017JD027006
- Moore, J. C., Rinke, A., Yu, X., Ji, D., Cui, X., Li, Y., ... Yang, S. (2014). Arctic sea ice and atmospheric circulation under the geomip g1 scenario. *Journal of Geophysical Research: Atmospheres*, *119*(2), 567–583. doi: https://doi.org/10.1002/2013JD021060
- Moore, J. C., Yue, C., Zhao, L., Guo, X., Watanabe, S., & Ji, D. (2019). Greenland Ice Sheet Response to Stratospheric Aerosol Injection Geoengineering. *Earth's Future*, *7*(12), 1451–1463. doi: https://doi.org/10.1029/2019EF001393
- Mouginot, J., Rignot, E., Bjørk, A. A., van den Broeke, M., Millan, R., Morlighem, M., ... Wood, M. (2019). Forty-six years of greenland ice sheet mass balance from 1972 to 2018. *Proceedings of the National Academy of Sciences*, *116*(19), 9239–9244. doi: 10.1073/pnas.1904242116
- National Academies of Sciences, Engineering, and Medicine. (2021). *Reflecting Sunlight: Recommendations for Solar Geoengineering Research and Research Governance*. Washington, DC: The National Academies Press. doi: 10.17226/25762
- Niemeier, U., Schmidt, H., & Timmreck, C. (2011). The dependency of geoengineered sulfate aerosol on the emission strategy. *Atmospheric Science Letters*, *12*(2), 189–194. doi: https://doi.org/10.1002/asl.304
- Notz, D., & SIMIP. (2020). Arctic sea ice in cmip6. *Geophysical Research Letters*,

- 47(10), e2019GL086749. doi: <https://doi.org/10.1029/2019GL086749>
- Notz, D., & Stroeve, J. C. (2018). The Trajectory Towards a Seasonally Ice-Free Arctic Ocean. *Current Climate Change Reports*, 4, 407–416. doi: 10.1007/s40641-018-0113-2
- Pierce, J. R., Weisenstein, D. K., Heckendorn, P., Peter, T., & Keith, D. W. (2010). Efficient formation of stratospheric aerosol for climate engineering by emission of condensable vapor from aircraft. *Geophysical Research Letters*, 37(18). doi: <https://doi.org/10.1029/2010GL043975>
- Pithan, F., & Mauritsen, T. (2014). Arctic amplification dominated by temperature feedbacks in contemporary climate models. *Nature Geoscience*, 7, 181–184. doi: <https://doi.org/10.1038/ngeo2071>
- Plaza, C., Pegoraro, E., Bracho, R., Celis, G., Crummer, K. G., Hutchings, J. A., ... Schuur, E. A. G. (2019). Direct observation of permafrost degradation and rapid soil carbon loss in tundra. *Nature Geoscience*, 12, 627–631. doi: 10.1038/s41561-019-0387-6
- Previdi, M., Smith, K. L., & Polvani, L. M. (2021, sep). Arctic amplification of climate change: a review of underlying mechanisms. *Environmental Research Letters*, 16(9), 093003. Retrieved from <https://doi.org/10.1088/1748-9326/ac1c29> doi: 10.1088/1748-9326/ac1c29
- Richter, J., Vioni, D., MacMartin, D., Bailey, D., Rosenbloom, N., Lee, W., ... Lamarque, J.-F. (2022). Assessing responses and impacts of solar climate intervention on the earth system with stratospheric aerosol injection (arise-sai). *EGU Sphere*, 2022, 1–35. doi: 10.5194/egusphere-2022-125
- Ridley, J. K., Lowe, J. A., & Hewitt, H. T. (2012). How reversible is sea ice loss? *The Cryosphere*, 6(1), 193–198. doi: 10.5194/tc-6-193-2012
- Robock, A., Oman, L., & Stenchikov, G. L. (2008). Regional climate responses to geoengineering with tropical and Arctic SO₂ injections. *Journal of Geophysical Research: Atmospheres*, 113(D16). doi: 10.1029/2008JD010050
- Schuur, E. A. G., McGuire, A. D., Schädel, C., Grosse, G., Harden, J. W., Hayes, D. J., ... E., V. J. (2015). Climate change and the permafrost carbon feedback. *Nature*, 520, 171–179. doi: 10.1038/nature14338
- Slater, D. A., Straneo, F., Felikson, D., Little, C. M., Goelzer, H., Fettweis, X., & Holte, J. (2019). Estimating greenland tidewater glacier retreat driven by submarine melting. *The Cryosphere*, 13(9), 2489–2509. doi: 10.5194/tc-13-2489-2019
- Smith, R., Jones, P., Briegleb, B., Bryan, F., Danabasoglu, G., Dennis, J., ... Yeager, S. (2010). The parallel ocean program (pop) reference manual, ocean component of the community climate system model (ccsm) [Computer software manual].
- Stroeve, J. C., & Notz, D. (2018, sep). Changing state of Arctic sea ice across all seasons. *Environmental Research Letters*, 13(10), 103001. doi: 10.1088/1748-9326/aade56
- Tarnocai, C., Canadell, J. G., Schuur, E. A. G., Kuhry, P., Mazhitova, G., & Zimov, S. (2009). Soil organic carbon pools in the northern circumpolar permafrost region. *Global Biogeochemical Cycles*, 23(2). doi: <https://doi.org/10.1029/2008GB003327>
- Tilmes, S., MacMartin, D. G., Lenaerts, J. T. M., van Kampenhout, L., Muntjewerf, L., Xia, L., ... Robock, A. (2020). Reaching 1.5 and 2.0°C global surface temperature targets using stratospheric aerosol geoengineering. *Earth System Dynamics*, 11(3), 579–601. doi: 10.5194/esd-11-579-2020
- Tilmes, S., Richter, J. H., Kravitz, B., MacMartin, D. G., Mills, M. J., Simpson, I. R., ... Ghosh, S. (2018, 12). CESM1(WACCM) Stratospheric Aerosol Geoengineering Large Ensemble Project. *Bulletin of the American Meteorological Society*, 99(11), 2361–2371. doi: 10.1175/BAMS-D-17-0267.1
- Vallis, G. K., Zurita-Gotor, P., Cairns, C., & Kidston, J. (2015). Response of the

- large-scale structure of the atmosphere to global warming. *Quarterly Journal of the Royal Meteorological Society*, 141(690), 1479-1501. doi: <https://doi.org/10.1002/qj.2456>
- van den Broeke, M., Box, J., Fettweis, X., Hanna, E., Noël, B., Tedesco, M., ... van Kampenhout, L. (2017). Greenland Ice Sheet Surface Mass Loss: Recent Developments in Observation and Modeling. *Current Climate Change Reports*, 3, 345–356. doi: 10.1007/s40641-017-0084-8
- Visioni, D. (2022). *Data from: Scenarios for modeling solar radiation modification*. Cornell eCommons Library. Retrieved from <https://doi.org/10.7298/xr82-sv86>
- Visioni, D., MacMartin, D. G., Kravitz, B., Lee, W., Simpson, I. R., & Richter, J. H. (2020). Reduced Poleward Transport Due to Stratospheric Heating Under Stratospheric Aerosols Geoengineering. *Geophysical Research Letters*, 47(17), e2020GL089470. (e2020GL089470 10.1029/2020GL089470) doi: 10.1029/2020GL089470
- Xie, M., Moore, J. C., Zhao, L., Wolovick, M., & Muri, H. (2022). Impacts of three types of solar geoengineering on the atlantic meridional overturning circulation. *Atmospheric Chemistry and Physics*, 22(7), 4581–4597. doi: 10.5194/acp-22-4581-2022
- Yang, Y., Wang, H., Smith, S. J., Easter, R. C., & Rasch, P. J. (2018). Sulfate aerosol in the arctic: Source attribution and radiative forcing. *Journal of Geophysical Research: Atmospheres*, 123(3), 1899-1918. doi: <https://doi.org/10.1002/2017JD027298>

Supporting Information for “High-latitude stratospheric aerosol injection to preserve the Arctic”

Walker Raymond Lee¹, Douglas G. MacMartin¹, Daniele Visoni¹, Ben Kravitz^{2,3}, Yating Chen⁴, John C. Moore^{4,5,6}, Gunter Leguy⁷, David M. Lawrence⁷, David A. Bailey⁷

¹Sibley School for Mechanical and Aerospace Engineering, Cornell University, Ithaca, NY, USA

²Department of Earth and Atmospheric Science, Indiana University, Bloomington, IN, USA

³Atmospheric Sciences and Global Change Division, Pacific Northwest National Laboratory, Richland, WA, USA

⁴College of Global Change and Earth System Science, Beijing Normal University, Beijing, 100875, China

⁵CAS Center for Excellence in Tibetan Plateau Earth Sciences, Beijing, 100101, China

⁶Arctic Centre, University of Lapland, Rovaniemi, Finland

⁷Climate and Global Dynamics Laboratory, National Center for Atmospheric Research, Boulder, CO, USA

Contents of this file

1. Text S1 and S2
2. Figures S1 to S5

Introduction Text S1 describes in more detail the feedforward/feedback control algorithm design process used to determine the injection rates for Arctic Low and Arctic High. Text S2 describes the statistical methods used to calculate standard error for multi-year averages for single simulations and ensembles with multiple members. Figures S1 and S2

show SW and LW fluxes; these figures are the same as Figures 2 and 3 in the manuscript, respectively, but with data for Arctic Low included. Figure S3 shows Atlantic Meridional Overturning Circulation (AMOC) data for Arctic Low, Arctic High, Global+1.5, and SSP2-4.5. Figure S4 shows column ozone changes as a function of season and latitude for Arctic High relative to SSP2-4.5. Figure S5 shows changes to Greenland for Arctic High relative to SSP2-4.5, including near-surface temperature, near-surface humidity, runoff, precipitation, and evaporation.

Text S1. The control algorithms used in the Arctic Low and Arctic High simulations consist of a feedforward term and a feedback term: the feedforward term, derived from previous simulations, estimates how much injection will be needed each year in order to meet the target September sea ice extent, and the feedback term applies a correction each year based on the difference between the actual and desired September sea ice extent during the simulation.

The feedforward gain is computed by estimating the linear increase in forcing needed to maintain the desired sea ice extent through our simulations. However, this is not as simple as finding the difference between sea ice in MAM-60 and RCP8.5 and dividing by injection rate because, during those simulations, the difference in sea ice extent is not proportional to changes in forcing; this is because September sea ice extent declines approximately linearly in 2000-2030 under RCP8.5 but nonlinearly by the MAM-60 simulation period of 2035-2045 (when September sea ice extent is close to 0). Therefore, in order for September sea ice differences in those simulations to be proportional to changes in forcing, we must extrapolate from the linear decline of 2000-2030 as in Lee, MacMartin, Visioni, and Kravitz (2020) and we compute a sensitivity of approximately 0.4 million km² of sea ice restored

per Tg of SO₂ injected (1 Tg = 1 Mt = 10¹² g). This results in a feedforward gain of 0.272 Tg/yr for Arctic Low and 6.109 Tg + 0.272 Tg/yr for Arctic High (with the offset in the Arctic High case to account for the sea ice difference between the reference time period of 2000-2020 and the first year of the simulation).

The feedback gain is computed using the MATLAB system identification toolbox, which, when provided an “input” and an “output”, can compute a relationship between them (referred to in feedback control theory as a “transfer function”) and then can compute feedback gains that produce a desired response. We define the MAM-60 injection rate of 12 Tg/yr as the input and the difference in September sea ice extent between MAM-60 and RCP8.5 as the output, and we specify an integral controller with a time constant of five years; this is the same time constant as the original design of Kravitz et al. (2017) and has been subsequently used in Tilmes et al. (2018, 2020); Richter et al. (2022); and MacMartin et al. (2022). This process computes a feedback gain of 0.491 Tg per year per million km², which is used in both Arctic Low and Arctic High (i.e., the injection quantity each year is adjusted up or down by 0.491 Tg for each million km² of the total time-integrated difference between model output and the target).

Text S2. 20-year averages are reported in the manuscript as $\mu \pm \delta$, where μ is the average and δ is the standard error. To compute the standard error for the 20-year average of a discrete timeseries, we approximate the timeseries $y(t)$ as a first-order autoregression, or AR(1), to account for interannual autocorrelation. An AR(1) approximation is given by the standard formula

$$y(t) = \beta_0 + \beta_1 y(t - 1) + \epsilon_t \quad (1)$$

where β_0 is a constant, β_1 is the correlation coefficient between $y(t)$ and $y(t-1)$, and ϵ_t is random noise. After computing β_0 and β_1 , we solve for ϵ for the latter 19 years of data using the above equation. We then compute

$$\delta = \sigma_\epsilon / \sqrt{(n_y - 1)} \quad (2)$$

where σ_ϵ is the standard deviation of the noise and $(n_y - 1) = 20 - 1 = 19$ degrees of freedom after the interannual autocorrelation has been removed.

For a simulation with multiple ensemble members, δ_{ens} for a 20-year average for the entire ensemble is a function of δ for each of the individual ensemble members. This is done using the standard error propagation formula

$$\delta_{ens} = \frac{\sqrt{\delta_1^2 + \dots + \delta_{n,ens}^2}}{n_{ens}} \quad (3)$$

with n_{ens} equal to the number of ensemble members (note that for an ensemble size of 1, $\delta = \delta_{ens}$). For a 20-year average of the difference between two ensemble members, δ_{diff} is found using the same error propagation formula

$$\delta_{diff} = \sqrt{\delta_{ens,1}^2 + \delta_{ens,2}^2} \quad (4)$$

Therefore, to compute (for example) the change in FSNT between Arctic High and SSP2-4.5 during the 2050-2069 period, as seen in Fig. 2a in the manuscript, we first compute the 20-year δ individually for the one ensemble member of Arctic High and each of the three ensemble members of SSP2-4.5 using Eqns. 1 and 2. We then compute δ_{ens} for SSP2-4.5 using Eqn. 3 with δ from each of the three ensemble members. Lastly, we

compute δ_{diff} using Eqn. 4 with $\delta = \delta_{ens}$ for the one ensemble member of Arctic High and δ_{ens} for SSP2-4.5.

References

- Kravitz, B., MacMartin, D. G., Mills, M. J., Richter, J. H., Tilmes, S., Lamarque, J.-F., ... Vitt, F. (2017). First Simulations of Designing Stratospheric Sulfate Aerosol Geoengineering to Meet Multiple Simultaneous Climate Objectives. *Journal of Geophysical Research: Atmospheres*, *122*(23), 12,616-12,634. doi: 10.1002/2017JD026874
- Lee, W., MacMartin, D., Vioni, D., & Kravitz, B. (2020). Expanding the design space of stratospheric aerosol geoengineering to include precipitation-based objectives and explore trade-offs. *Earth System Dynamics*, *11*(4), 1051–1072. doi: 10.5194/esd-11-1051-2020
- MacMartin, D. G., Vioni, D., Kravitz, B., Richter, J. H., Felgenhauer, T., Lee, W. R., ... Sugiyama, M. (2022). Scenarios for modeling solar radiation modification. *Proceedings of the National Academy of Sciences of the United States of America*.
- Richter, J., Vioni, D., MacMartin, D., Bailey, D., Rosenbloom, N., Lee, W., ... Lamarque, J.-F. (2022). Assessing responses and impacts of solar climate intervention on the earth system with stratospheric aerosol injection (arise-sai). *EGUsphere*, *2022*, 1–35. doi: 10.5194/egusphere-2022-125
- Tilmes, S., MacMartin, D. G., Lenaerts, J. T. M., van Kampenhout, L., Muntjewerf, L., Xia, L., ... Robock, A. (2020). Reaching 1.5 and 2.0°C global surface temperature targets using stratospheric aerosol geoengineering. *Earth System Dynamics*, *11*(3), 579–601. doi: 10.5194/esd-11-579-2020
- Tilmes, S., Richter, J. H., Kravitz, B., MacMartin, D. G., Mills, M. J., Simpson, I. R.,

... Ghosh, S. (2018, 12). CESM1(WACCM) Stratospheric Aerosol Geoengineering Large Ensemble Project. *Bulletin of the American Meteorological Society*, 99(11), 2361-2371. doi: 10.1175/BAMS-D-17-0267.1

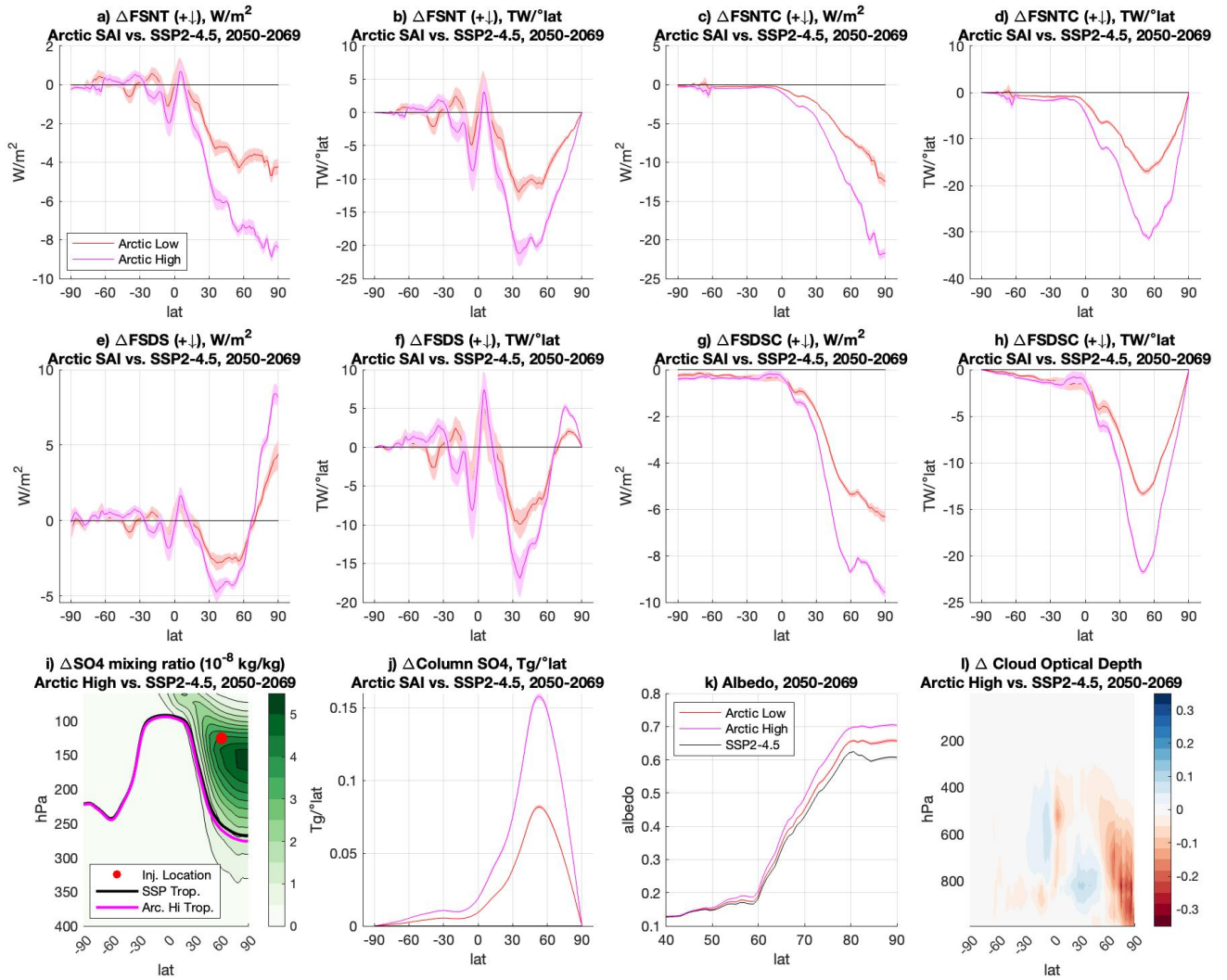


Figure S1. Changes to shortwave (SW) fluxes, sulfur burden, surface albedo, and cloud optical depth. This figure is identical to Fig. 2 in the manuscript, but with Arctic Low included for panels a-h and j-k.

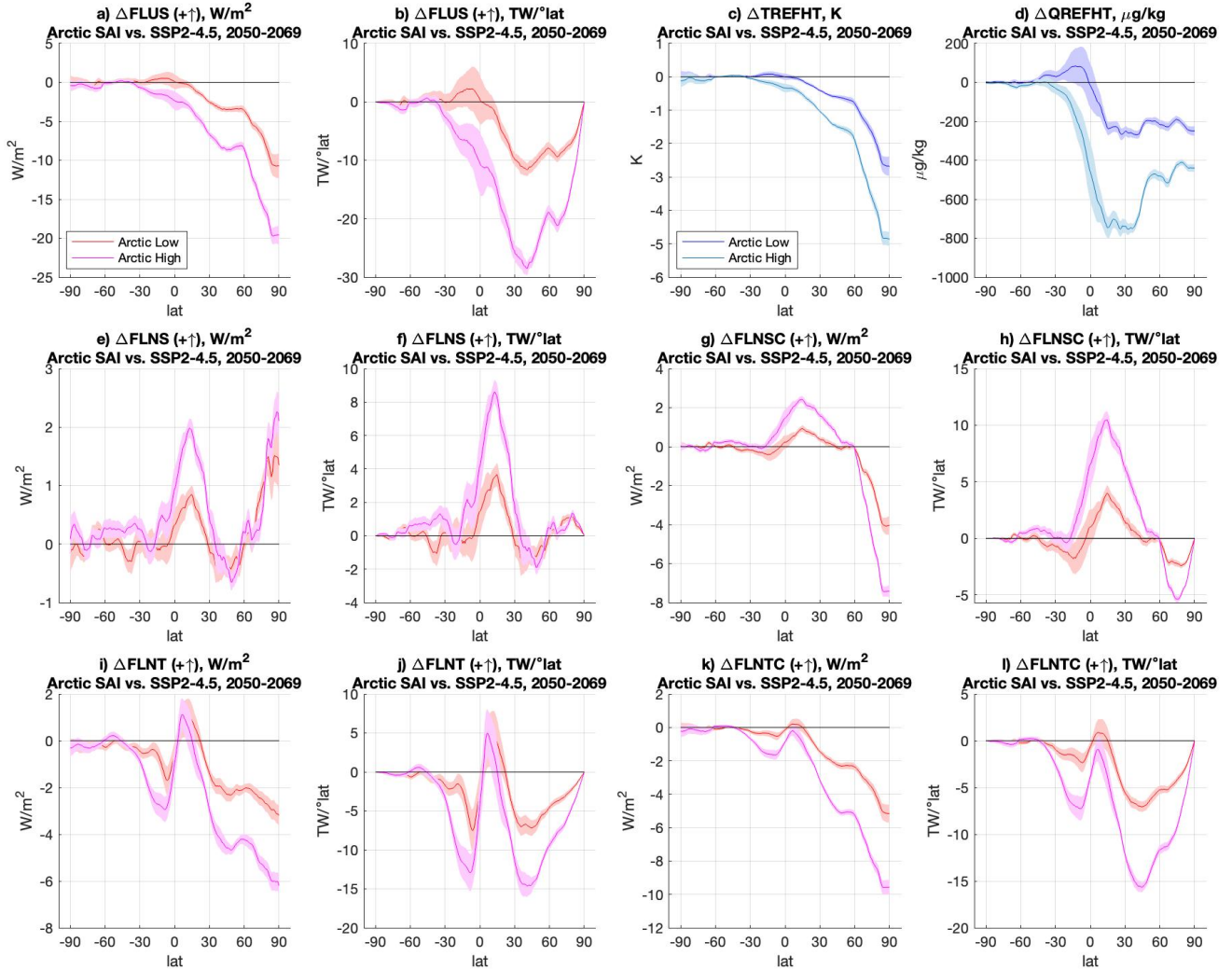


Figure S2. Changes to shortwave (LW) fluxes, surface temperature, and near-surface humidity.

This figure is identical to Fig. 3 in the manuscript, but with Arctic Low included for all panels.

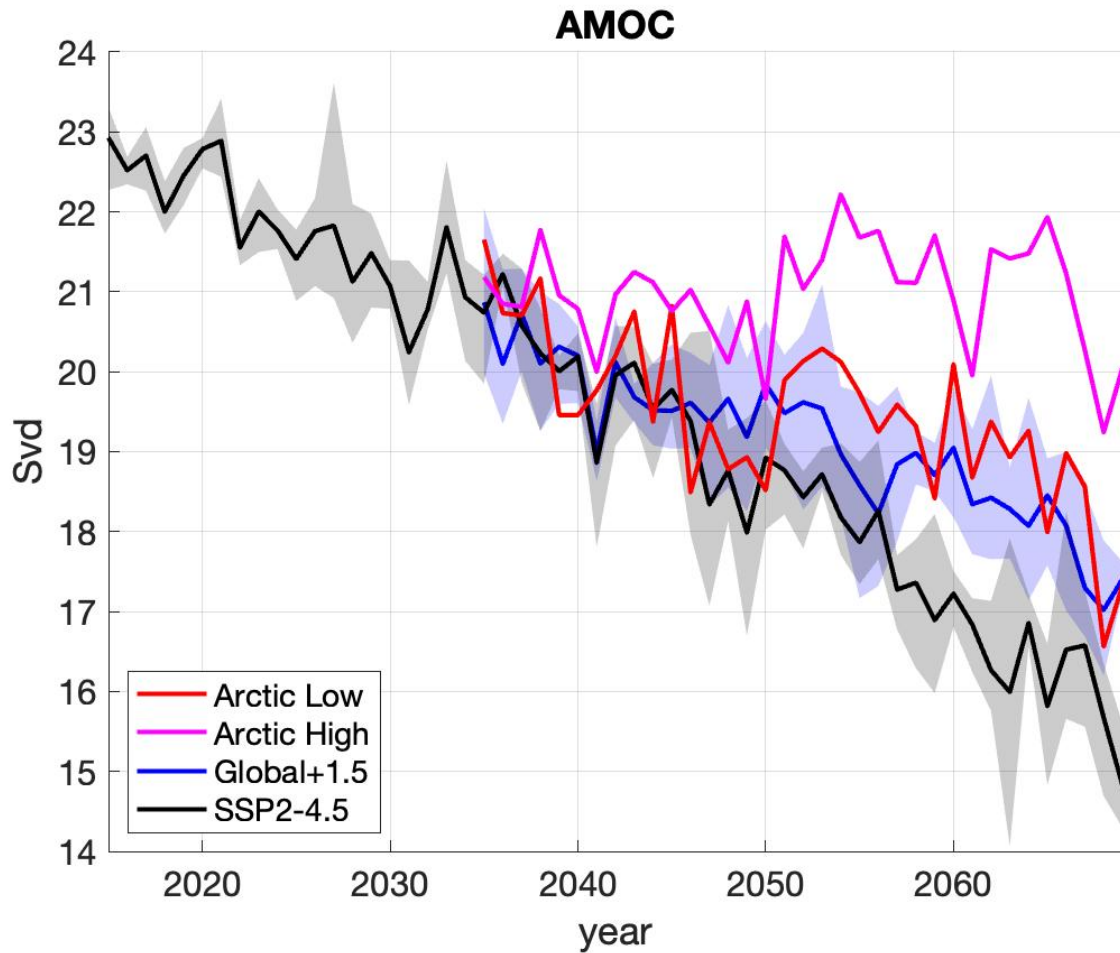


Figure S3. Strength of the Atlantic Meridional Overturning Circulation (AMOC) over time for Arctic SAI, Global+1.5, and SSP2-4.5. Shading for Global+1.5 and SSP2-4.5 denotes ensemble spread.

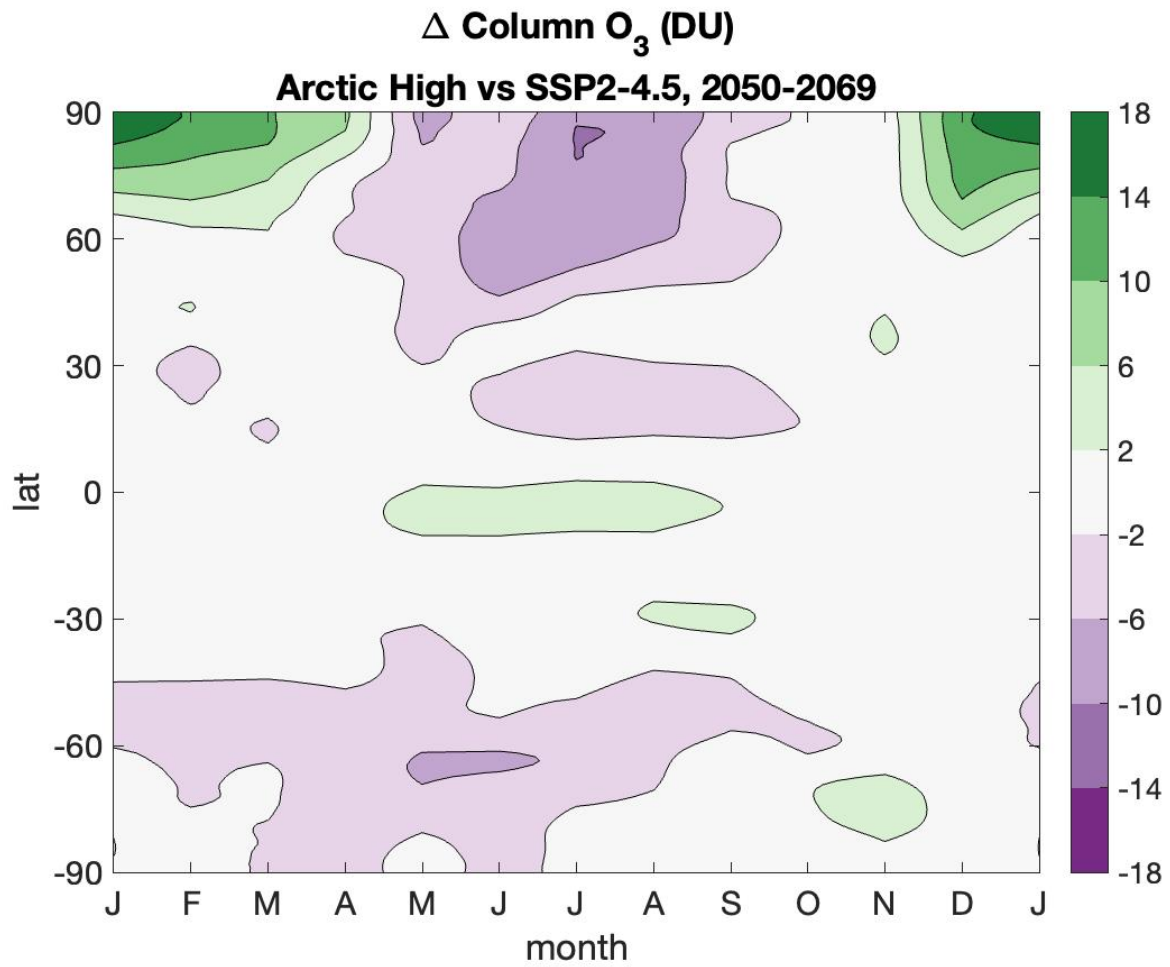


Figure S4. Changes to the zonal mean seasonal cycle of atmospheric column ozone burden for Arctic High relative to SSP2-4.5, averaged over the 2050-2069 period.

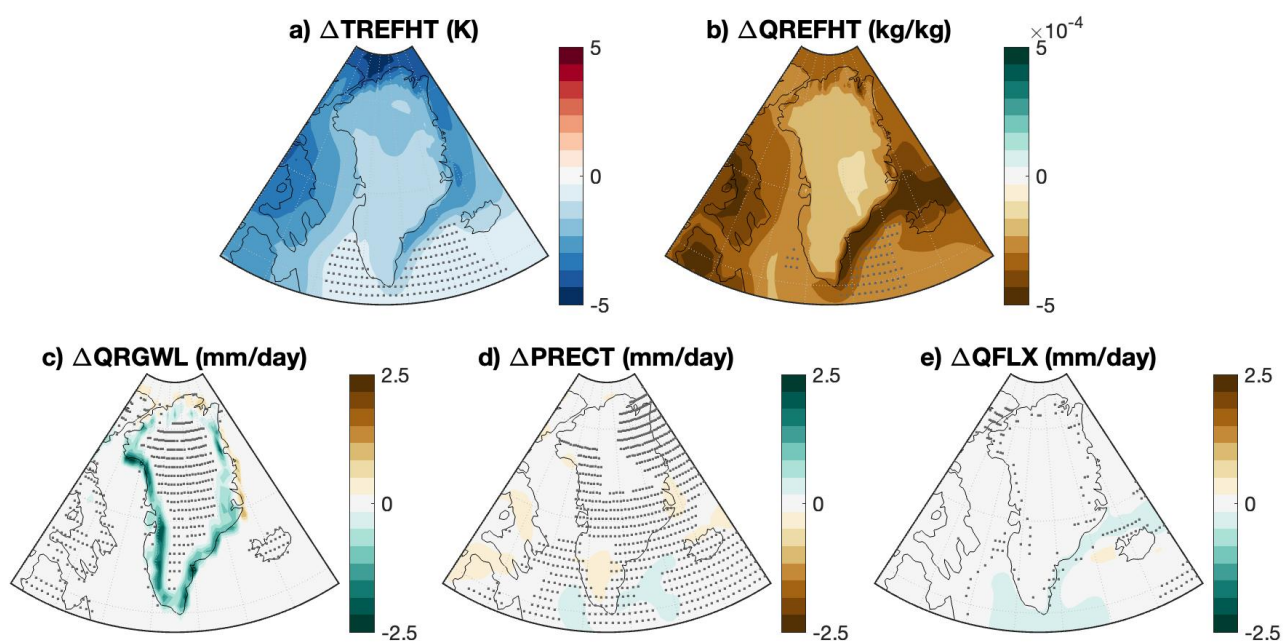


Figure S5. Maps of changes to near-surface temperature (a), near-surface humidity (b), runoff (c), precipitation (d), and evaporation (e) for Arctic High relative to SSP2-4.5, averaged over the 2050-2069 period. Stippling indicates areas with no significant change according to the two-sample t-test at the 95% confidence level.